National Research Council Canada
Conseil national de recherches Canada

AN EXPERIMENTAL STUDY OF THE TRANSONIC EQUIVALENCE RULE WITH LIFT

by
Y.Y. Chan
National Aeronautical Establishment

OTTAWA
MARCH 1982

Canada

AERONAUTICAL REPORT
LR-609
NRC NO. 20225

AN EXPERIMENTAL STUDY OF THE TRANSONIC EQUIVALENCE RULE WITH LIFT

ÉTUDE EXPÉRIMENTALE DE L'APPLICATION À LA PORTANCE DE LA RÈGLE D'ÉQUIVALENCE TRANSSONIQUE

by/par

Y.Y. Chan

L.H. Ohman, Head/Chef
High Speed Aerodynamics Laboratory/
Laboratoire d'aérodynamique à hautes vitesses

G.M. Lindberg
Director/Directeur

SUMMARY

The transonic equivalence rule with lift has been studied experimentally. Under the conditions defined by the rule, wing-body models with the same cross-sectional area distribution but with wings of different aspect ratios and thicknesses were tested at transonic speeds. The correlations of the lift depending wave drag and the lift parameter for the models are found to be similar. The similitude of the outer flow field under the same lifting condition is also established. The drag-rise of the equivalent body of revolution with the cross-sectional area distribution including that due to lift correlates well with those of the wing-body models at the design lift condition. The experiment therefore verifies the transonic equivalence rule at lifting condition.

RÉSUMÉ

On a étudié expérimentalement l'application à la portance de la règle d'équivalence transsonique. Dans les conditions définies par la règle, des profils aérodynamiques ayant la même distribution de section transversale mais des allongements et des épaisseurs différents ont été soumis à des essais à des vitesses transsoniques. On a trouvé pour le paramètre de portance et la traînée d'onde, liée à la portance, des corrélations similaires entre les modèles considérés. On a aussi établi la similitude des champs d'écoulement extérieurs dans les mêmes conditions de portance. Il y a une bonne corrélation entre l'augmentation de traînée du corps de révolution équivalent, en ce qui a trait à la distribution de section transversale incluant celle due à la portance, et celle des profils, aux conditions de portance théorique. L'expérience permet donc de vérifier la validité de la règle d'équivalence transsonique aux conditions de portance.

CONTENTS

TABLES

ILLUSTRATIONS

ILLUSTRATIONS (Cont'd)

APPENDICES

SYMBOLS

Symbol	Definition
a	contour of the leading edge of the wing planform, Equation (14)
a	speed of sound, Equation (A5)
A	aspect ratio of the wing
b	semi-space of the wing
c	chord length of the wing section
c_o	root chord of the wing
C_D	drag coefficient
$\bar{C}_D$	$C_D - C_{D_m}$, Equation (A28)
$\Delta\bar{C}_D$	$\Delta C_{D_o} + \bar{C}_{D_w}$, with reference to the maximal cross-section area, Figure 22
C_{D_i}	induced drag coefficient
C_{D_m}	minimum of drag coefficient
C_{D_o}	drag coefficient at zero lift, same as C_{D_m}
ΔC_{D_o}	$C_{D_o} - C_{D_{o,M=0.8}}$, Figure 7
$\bar{C}_{D_w}$	wave drag coefficient, Equation (13)
C_L	lift coefficient
$\bar{C}_L$	$C_L - C_{L_m}$, Equation (A28)
C_{L_m}	C_L at C_{D_m}
C_{L_α}	lift curve slope
$C_{L_{\alpha_o}}$	lift curve slope at zero lift
C_p	pressure coefficient
D_o	doublet strength, Equation (2)
D_w	wave drag, Equation (11)
E	cross-flow integral, Equation (7)
F	axial lift distribution, Equation (5)

SYMBOLS (Cont'd)

Symbol	Definition
h	half height of the wind tunnel test section
k	induced drag factor, Equation (28)
$\tilde{k}$	induced drag factor, Equation (30)
K	transonic similarity parameter for wing-body combination, Equation (1)
K_b	transonic similarity parameter for body of revolution, Figure 7
ℓ	body length
M	Mach number
P	wind tunnel wall porosity factor
S_b	cross-sectional area of the central body, Equation (22)
S_c	geometric cross-sectional area, Equation (8)
S_e	effective cross-sectional area, Equation (3)
t	maximal thickness of the wing-section
T	axial-flow integral, Equation (16)
U_∞	free stream velocity
u,v,w	velocity components in the x, y, z — directions respectively
x,r,w	polar co-ordinates
x,y,z	Cartesian co-ordiantes
α	angle of attack
$\bar{\alpha}$	$\alpha - \alpha_m$, Equation (A18)
α_m	α at C_{D_m}
α_e	lift parameter Equation (8)
γ	ratio of specific heat
δ	thickness of the body, Equation (A3)
ϵ	ratio of the transverse length scales, Equation (4)
η	scaled transverse co-ordinates, Equation (9)

SYMBOLS (Cont'd)

Symbol	Definition
λ	wing sweep parameter, Equation (8)
ρ	density
τ	body thickness parameter, Equation (8)
τ_b	slender ratio for body of revolution, maximal diameter/ℓ
ϕ	velocity potential

Subscript

∞	free stream condition

AN EXPERIMENTAL STUDY OF THE TRANSONIC EQUIVALENCE RULE WITH LIFT

1.0 INTRODUCTION

In the last two decades, the transonic area rule has played an important role in the design of high speed aircraft. The rule indicates the relation between the transonic drag rise and the cross-sectional area distribution of the aircraft, allowing the configuration to be designed with niminal drag rise. The principle of the rule is based on the properties of the air moving at a speed near the speed of sound. At Mach number close to unity, the air flow will resist any streamtube area change with a large force. To avoid large perturbation pressures and hence high drag, the changes of the cross-sectional area should therefore be gradual and smooth. The constraint of the stream-tube effectively causes the cross-flow in planes normal to the free-stream direction to behave like an imcompressible flow. This allows the nonlinear transonic flow field to be analyzed asymptotically leading to the formulation of the area rule.

The analysis shows that the far field is governed by the transonic small disturbance theory. The cross-flow near the body tends to be incompressible as in the case of the flow near a slender body and hence can be treated in a similar manner. To the far field, the displacement effect of the body appears as that generated by a line source distributed along the axis of the body and is thus identical to that of an axisymmetrical body having the same cross-sectional area distribution. This similitude of the displacement effect is basically the equivalence rule or the area rule[1,2]. The concept was verified experimentally by Whitcomb[3] and has since been applied to aircraft design for drag reduction at transonic speeds.

When the aircraft is in lifting condition the transonic flow past the wing causes further expansion of the streamtube. To the far field the lift distribution along the body axis is represented by a line doublet and the expansion of the streamtube appears as additional sources which relate directly to the lift distribution. To form the equivalence body, the effective area representing these additional sources must be added to the geometric cross-sectional area. The basic idea was incorporated in the design of an early experiment of transonic transport aircraft, but the amount of lift compensation area was then derived entirely empirically. Theoretical analysis of this problem was later carried out by Cheng and Hafez[5], and Barnwell[6,7]. In their analysis the detailed structure of the flow is delineated and the conditions of the similitude of the far fields are established. The explicit expressions of the doublet and source strengths induced by lift given in the analysis are particularly important for engineering applications. This has been demonstrated in a design study of transonic transport aircraft[8], and the estimations of drag-rise for configurations of fighter-type aircraft[9].

The extended equivalence rule with lift can be expressed in a form of flow similitude. It states that flows having the same distributions of sources $S_e'(x)$ and doublets $D_o(x)$, with the same transonic similarity parameter K are equivalent. The nonlinear structure of the flow field including the formation of shock-waves and the associated drag-rise will be identical. The parameters controlling the lift effect and the geometry of the body do not appear explicitly and it is therefore more general than the classical transonic similarity law[10].

The present study attempts to establish the similitude of the flow fields according to the extended equivalence rule. Two wing-body models are designed with the wings having different thicknesses and aspect ratios but the same cross-sectional area distributions. The models are tested at incidences through the transonic Mach number range. The lift and the drag forces acting on the models are measured and the static pressure variation at the far field is also monitored in the experiment. The data are then examined in the parametric forms defined by the equivalence rule. The main parameter chosen for detailed study is the lift-depending drag associated with the shock wave formation. The result shows that for the same transonic condition, the correlations of the wave drag and the lift parameter for the two models are similar. Comparisons of far field pressure distributions and shock patterns for the two models also indicate similarity of the flow fields. Thus the flow similitude defined by the equivalence rule is obtained.

Two equivalent bodies of revolution corresponding to the conditions of zero lift and of finite lift respectively are also part of the experiment. In both cases the drag-rise of the equivalent bodies correlates very well with those of the wing-bodies at the design conditions. The latter result verifies the effective displacement of the flow due to lift as defined by the extended equivalence rule.

In the report, the theoretical results of the extended equivalence rule is first outlined. The design of the models for the experiment is then described. The experimental procedure and the data are presented in some details. Finally, the data are analyzed in the parametric forms defined by the equivalence rule and the conditions of flow similitude are then established.

2.0 TRANSONIC EQUIVALENCE RULE WITH LIFT

Transonic flows past a three-dimensional configuration have been analyzed by Cheng and Hafez, leading to the establishment of the equivalence rule with lift[5]. The analysis shows that at a specified transonic similarity parameter K, the outer flow is uniquely determined by a line doublet distribution $D_o(x)$ due to lift and a line source distribution $S_e'(x)$ related to both lift and displacement of the body. Flows having the same distributions of $D_o(x)$ and $S_e'(x)$, with the same value of K are therefore equivalent. These parameters are given as follows:

$$K = \frac{M_\infty^2 - 1}{(\gamma + 1) M_\infty^2 \tau \lambda} \tag{1}$$

$$D_o(x) = \sigma_* |\ell n\, \epsilon|^{-1/2} F(x) \tag{2}$$

$$S_e'(x) = \frac{d}{dx}\left\{S_c(x) + \sigma_*^2 \left[\frac{1}{8\pi}\left(1 + \frac{1}{2}|\ell n\, \epsilon|^{-1}\right) F_x^2 + \frac{1}{2}|\ell n|^{-1} T(x) + \frac{1}{8}\Gamma^* E(x)\right]\right\} \tag{3}$$

where

$$\begin{aligned} \sigma_* &= (\gamma + 1)^{1/2}\ M_\infty |\ell n\, \epsilon|^{1/2}\ \alpha_\ell\ \lambda^{3/2}\ \tau^{-1/2} \\ \Gamma_* &= 8(\gamma + 1)^{-1}\ \lambda^{-2}\ |\ell n\, \epsilon|^{-1} \\ \epsilon &= [(\gamma + 1) M_\infty^2\ \tau \lambda^3]^{1/2} \end{aligned} \tag{4}$$

and

$$F(x) = \int_{-\infty}^{\infty} [\varphi(x, y)]\, dy$$

$$T(x) = \frac{1}{4\pi} \int_{-\infty}^{\infty} \int_{-\infty}^{\infty} [\varphi(x, y)]_x\ [\varphi(x, s)]_x\ \ell n \left|\frac{1}{y - s}\right| dy\, ds \tag{6}$$

$$E(x) = \frac{1}{4\pi} \int_{-\infty}^{\infty} \int_{-\infty}^{\infty} [\varphi(x, y)]_y\ [\varphi(x, s)]_y\ \ell n \left|\frac{1}{y - s}\right| dy\, ds \tag{7}$$

The basic parameters are defined as

$$\tau = \frac{S^*_{max}}{b\ell}, \qquad \alpha_\ell = \frac{F^*_{max}}{\rho_\infty U_\infty^2 b^2}, \qquad \lambda = \frac{b}{\ell} \tag{8}$$

and the outer region of the flow is scaled as

$$x = \frac{x^*}{\ell} , \qquad \eta = \frac{\epsilon r^*}{b} , \qquad \omega \tag{9}$$

where the superscript * denotes quantities with physical dimensions, ℓ is the body length, b the semispan of the wing and ϵ the ratio of the transverse length scales for the inner and the outer regions of the flow field. S^*_{max} and F^*_{max} are the maximum cross-sectional area and the maximum of the local lift force F^* (x) respectively. Thus τ is the parameter of thickness of the configuration, α_ℓ the lift and λ the wing sweep parameters. The parameters controlling the lift effects on the outer flow are σ_* and Γ_*. $D_o(x)$ is the line doublet due to lift and $S_e'(x)$ is the line source in the form of the first derivative of the effective cross-sectional area consisting of the geometric cross-sectional area $S_c(s)$ and the contributing due to lift. The first term of the lift effect in the square bracket of Equation (3) is from the axial distribution of the lift force F(x). The last term E(x) signifies the cross-flow kinetic energy, comparable to induced drag and is finite in the wake region.

When the flow fields are equivalent, the local pressure coefficient and the Mach number are functions of the transonic similarity parameter K only

$$\frac{C_p}{\tau\lambda} , \frac{M^2 - 1}{\epsilon^2} = f(x, \eta, \omega; K) \tag{10}$$

Hence the drag-rise associated with the shock waves is also a function of K

$$D_w / (\rho_\infty U_\infty^2 b^2 \tau^2 M_\infty^2) = f(K) \tag{11}$$

The conditions of the equivalence rule as given in Equations (1), (2) and (3) are much less restricted than the classical transonic similitude. The parameters controlling the lift σ_* and the wing geometries for the equivalent flows do not require to be the same.

We have summarized the results of the extended equivalence rule with lift as given in Reference 5. The parameters shown in Equations (1) to (4) are complicated in form, but it is not difficult to trace their relations to the respective physical quantities. The basic form of these parameters can be derived from the similarity analysis of the transonic small disturbance equation. This exercise does help us to understand the formation of these parameters and their physical implications and is therefore included in the report as Appendix A.

3.0 DESIGN OF THE EXPERIMENT

The purpose of the experiment is to establish the flow field similarity according to the equivalence rule at lifting condition. This is done by correlating the flow parameters in the form defined by the equivalence rule and if the correlations for different models are similar, then the flow fields are equivalent. With the understanding that the ultimate application of the equivalence rule is to reduce the drag-rise caused by the formation of shock-waves, the lift dependent wave drag is chosen as the main parameter for the present study. Its direct association with the shock formation in the outer field provides a measure of the nonlinear features in the region. In addition the static pressure variation in the far field is also monitored to add further information for the establishment of flow similitude.

Two wing-body models are designed for the experiment. The wings of the models have different thickness and aspect ratio and are mounted at the central plane of a cylindrical body housing an internal balance for force measurements. In the design of the models the functual forms relating to the parameters given in Equations (2) and (3) must be considered. These relations are now written in terms of the similarity parameters discussed in the Appendix A for a better understanding of their physical implications.

$$D_o(x) = \epsilon \frac{\alpha_\ell}{\tau} F(x) \tag{12}$$

$$S_e(x) = S_c(x) + \frac{1}{2}\left(\epsilon\frac{\alpha_\ell}{\tau}\right)^2\left[\frac{2\,|\,\ell n\,\epsilon\,|\,+1}{8\pi}\,F_x^2(x) + T(x) + \frac{2}{(\gamma+1)\lambda^2}\,E(x)\right] \tag{13}$$

The sectional profile of the wings is chosen symmetrical so that the lift effect can be simply related to the angle of attack. The wing planforms are selected to be geometrically similar so that the functions F(x), T(x) and E(x) are the same for both models. If the planforms are not geometrically similar, it is necessary to solve inversely from Equations (5) to (7) for the planform shape of the second model if the first one is initially specified. For geometrically similar planforms the condition $D_o(x)$ being the same is satisfied, if the parameter $\epsilon\,\alpha_\ell/\tau$ is identical for both models (see Eq. (12)). The condition $S_e(x)$ being identical requires that the parameters ϵ and λ are the same for the two models respectively. This leads to the trivial case that the two planforms are exactly identical. However, if the function F_x^2 is proportional to the function E(x), then a functional relationship can be established for ϵ and λ satisfying the desired similarity condition of $S_e(x)$. The effective areas can thus be kept identical for the two models but with different sweep back parameters. From the slender wing theory it can be shown that only a delta planform satisfied this condition. Thus the delta planform is adopted for the model design. The evaluations of the functions F(x), T(x) and E(x) for a planar wing at angles of attack are given in Appendix B and the results are summarized as follows:

$$\begin{aligned} F(x) &= a^2 \\ F_x^2(x) &= 4\,a^2\,a_x^2 \\ T(x) &= \frac{1}{\pi}\,\ell n\left(\frac{2}{a}\right)a^2\,a_x^2 \\ E(x) &= \frac{1}{2\pi}\,a^2 \end{aligned} \tag{14}$$

where a(x) is the leading edge contour. The expressions have been normalized by the value of F(x) at the trailing edge. For a delta wing a_x is unity and F_x^2 is thus proportional to E(x).

3.1 Planform Design

The respective relations of λ, τ, α and M_∞ for two wings are now determined in the following procedure. The geometric cross-section $S_c(x)$ is made identical for both models, since the lengths of the models are the same. Thus from the definitions in Equation (8), we have

$$\tau_1\lambda_1 = \tau_2\lambda_2 \tag{15}$$

which determines the relative thickness and aspect ratio of the wings. The condition that the transonic similarity parameter K being identical leads to the Mach number relation

$$M_{\infty_1} = M_{\infty_2} \tag{16}$$

From the definition of ϵ, we thus have

$$\frac{\epsilon_1}{\epsilon_2} = \frac{\lambda_1}{\lambda_2} \tag{17}$$

The requirement that the doubled strength distribution $D_o(x)$ is the same implies from Equation (12) that $\epsilon\,\dfrac{\alpha_\ell}{\tau}$ assumes the same value for both wings,

$$\epsilon_1\,\frac{\alpha_{\ell_1}}{\tau_1} = \epsilon_2\,\frac{\alpha_{\ell_2}}{\tau_2} \tag{18}$$

With this condition and the properties of delta wing given in Equation (14) the requirement that the effective area induced by lift is the same leads, from Equation (13), to the relation

$$\frac{\epsilon_1}{\epsilon_2} = \exp\left[\frac{1}{\gamma+1}\left(\frac{1}{\lambda_2^2} - \frac{1}{\lambda_1}\right)\right] \tag{19}$$

With Equation (17) a relation between λ_1 and λ_2 is obtained

$$\lambda_1^2 = \frac{\left(\frac{\lambda_1}{\lambda_2}\right)^2 - 1}{(\gamma+1)\,\ell n\left(\frac{\lambda_1}{\lambda_2}\right)} \tag{20}$$

In the design λ_1 is specified and λ_2 is determined from Equation (20). The relation between τ_1 and τ_2 follows from Equation (15) and between α_{ℓ_1} and α_{ℓ_2} from Equation (18).

3.2 Wing Section

A symmetric airfoil section based on Boerstoel's designs[13,14] is used for the wing section. The nose shape of the original section has been modified to eliminate the peaky pressure rise[15]. The sectional shape is scaled to the required thickness of the model. The coordinates of the airfoil is given in Table 1 for thickness-chord ratio of 0.1. Typical calculated pressure distribution on the upper and the lower surface of the airfoil at angle of attack is shown in Figure 1. The pressure near the nose region decreases monotonically and there is no pronounced suction peak. This condition is required for the existence of the solution, which leads to the equivalence rule[5,8].

3.3 Wing Tip Round Off

The equivalent body shape as given in Equation (13) depends on the functions F_x, E(x) and T(x) when the model is in lifting condition. For a delta wing, all these functions will be discontinuous at the trailing edge of the wing leading to a discontinuity of the equivalent body contour. In order to smooth the equivalent body shape (as the trailing edge position is approached) to prevent adverse effects on the boundary layer flow, the wing tip is shaped as a sine function to allow the slope of the leading edge contour to decrease gradually to zero. The contour is given as

$$\frac{y}{b} = 0.0637 \sin\left[\frac{\pi}{2}\left(\frac{\frac{x}{c} - 0.9}{0.1}\right)\right] \qquad \begin{matrix} 0.9 \leqslant \frac{a}{c} \leqslant 1, \\ 0.9 \leqslant y/b \end{matrix} \tag{21}$$

The contouring of the wing tip is in contradiction to the similarity requirement as discussed at the beginning of Section 3. However, since only a small portion of the wing planform has been altered, the effect to the outer flow field is small and the similarity of the flow can still be established.

3.4 Wing-body Combination

For a wing-body combination the parameter scaled to the wing-body can be related to those scaled to the wing alone[8]. If the length scale ℓ denotes the body length and τ_o is the root chord of the wing, thus the following relations can be established

$$\tilde{\lambda} = \frac{c_o}{\ell}\lambda \qquad \tilde{\tau} = \frac{c_o}{\ell}\left(\tau + \frac{S_b}{b\,c_o}\right) \qquad \tilde{\alpha}_\ell = \alpha_\ell \tag{22}$$

and with

$$\tilde{x} = \frac{x}{\ell}, \quad \bar{x} = \frac{x - x_o}{c_o};$$

$$\tilde{F}^2_{\tilde{x}} = \left(\frac{\ell}{c_o}\right)^2 F^2_{\bar{x}}$$

$$\tilde{T}(\tilde{x}) = \left(\frac{\ell}{c_o}\right)^2 T(\bar{x}) \tag{23}$$

$$\tilde{E}(\tilde{x}) = E(\bar{x})$$

Equations (12) and (13) become

$$\tilde{D}_o(\tilde{x}) = \tilde{\epsilon}\frac{\tilde{\alpha}_\ell}{\tilde{\tau}}\left(\frac{\ell}{c_o}\right)^2 F^2_{\bar{x}} \tag{24}$$

$$\tilde{S}_e(\tilde{x}) - \tilde{S}_c(\tilde{x}) = \frac{1}{2}\left(\tilde{\epsilon}\frac{\tilde{\alpha}_\ell}{\tilde{\tau}}\right)^2\left(\frac{\ell}{c_o}\right)^2\left[\frac{2\,|\ell n\,\tilde{\epsilon}\,| + 1}{8\pi} F^2_{\bar{x}} + T(\bar{x}) + \frac{2}{(\gamma+1)\lambda^2} E(\bar{x})\right] \tag{25}$$

where x_o is the location of the apex of the wing planform along the body axis. The expression inside the square bracket of Equation (25) is the same as the wing alone case Equation (13), except that the scaling parameter is now $\tilde{\epsilon}$. The conditions discusses in Section 3.1 can be applied to the wing-body case as

$$\tilde{\tau}_1\tilde{\lambda}_1 = \tilde{\tau}_2\tilde{\lambda}_2$$

$$\frac{\tilde{\epsilon}_1}{\tilde{\epsilon}_2} = \frac{\tilde{\lambda}_1}{\tilde{\lambda}_2} \tag{26}$$

and the $\tilde{\lambda}$ relation in Equation (20) still applies. The wings can therefore be adopted to the wing-body model without alteration.

The nose contour of the central body is a von Karman ogive which gives minimum drag for a given base area at supersonic speed. The nose shape is not optimized at transonic speeds and a shock will be formed at the end of the nose portion.

The dimensions and the parameters of two models are given in Table 2. The general layout of the models is shown in Figure 2. Since model WB1 has a thicker wing and a larger portion of the wing relative to the span is covered by the central body the cross-section area of the wing (excluding the part inside the body) is smaller than that of model WB2 at the corresponding section. The central body of the model WB1 is thus enlarged slightly to compensate for the area defect of the wing so that the total area of the wing-body is the same for both models. The cross-sectional area distribution is shown in Figure 3.

For a configuration with thin wing and slender body the classical area rule is applicable for the parameter $2\lambda\left(\frac{t}{\ell}\right)^{1/3}$ less than unity[16,17]. The present models have values of 0.2 and 0.3 respectively and are well within the range of application.

3.5 Equivalent Bodies

At zero lift, an equivalent body can be simply designed to have the same cross-sectional area distribution as the wing-body models. An axisymmetric model, B1, has been designed for this condition to check whether the classical area rule applies for the present models. When the wing-body

is at lifting condition, the effective area due to lift as given by the right-hand side of Equation (25) should be added to the geometric area. The parameter controlling the lift is $\tilde{\epsilon}\tilde{\alpha}_\ell/\tilde{\tau}$ as indicated in Equation (24). An equivalent body can therefore be designed for a lifting condition with specific $\tilde{\epsilon}\tilde{\alpha}_\ell/\tilde{\tau}$ and $\tilde{\epsilon}$. To study the drag-rise at a specified lift condition, the lift parameter $\tilde{\epsilon}\tilde{\alpha}_\ell/\tilde{\tau}$ must be kept constant as Mach number increases. However, $\tilde{\epsilon}$ is a function of Mach number and the effective area defined in Equation (25) depends on $\tilde{\epsilon}$. Thus a series of axisymmetric equivalent bodies would be needed to cover a Mach number range for the lifting condition. We also note that $\tilde{\epsilon}$ appears in the form $|\ell n\,\tilde{\epsilon}|$ in Equation (25) and within the range of Mach number of 0.8 to 1.1, $|\ell n\,\tilde{\epsilon}|$ varies less than 10 percent. The corresponding effect on the maximum cross-sectional area is only 2.5 percent. Thus for this experiment only one axisymmetrical body is designed at a specified lift condition and the same model is used to study the drag-rise through the Mach number range. The conditions chosen for the design are as follows.

$$\frac{\tilde{\epsilon}\tilde{\alpha}_\ell}{\tilde{\tau}} = 0.2024, \qquad \tilde{\epsilon}_1 = 0.0381$$

which corresponds to the wing-body model WB1 at the conditions

$$M_\infty = 0.975, \qquad C_L = 0.37$$

These conditions are chosen to simulate a lifting condition at cruise of a typical transonic aircraft (see Ref. 8). The angle of attack of the aircraft would be 5 degrees based on slender wing theory. The effective area due to lift is also shown in Figure 2. The added area on the aft-body is caused by the cross-flow kinetic energy in the wake, a finite contribution from the function $E(\tilde{x})$.

The models are designed to have a central basic body for housing the internal balance. An outer body consisting of the wing-body or the equivalent body is slid over the central body to provide the proper contour. For the lifting equivalent body a sleeve is slid over the aft-body to increase the cross-sectional area as required. A nose portion common to all models is then installed to complete the configuration. The general layout of the model parts before assembly is shown in Figure 4.

It has been found in Reference 18 that there is no essential difference on transonic drag-rise of the wing with and without boundary layer tripping. Thus in this experiment, performed at reasonably high Reynolds number, no boundary layer tripping is applied on the wing and the nose of the body of the models.

3.6 Flow Similarity Within a Wind Tunnel

Since the experiment will be performed in a wind tunnel, the effect of the tunnel walls to the flow past the model must be considered. The severity of the constraint of the tunnel wall can be estimated by comparing the physical dimensions of the working section and the length scales of the flow field. The transverse length scale of the outer region of the flow is $b/\tilde{\epsilon}$ and has a value of 106 inches (2.69 m) for the present wing-body model and the design conditions discussed in the last section. The wind tunnel has a 60-inch (1.5 m) square working section. Thus the tunnel wall interference cannot be treated as a weak correction and the walls should be considered as an integral part of the flow boundary.

For the flows within the tunnel to be similar for both models the length scales in both the longitudinal and the transverse directions must be the same respectively. The first condition is satisfied since the models have the same length. The second condition follows from the second design condition specified in Equation (26), giving identical transversal length scales. Since the walls are now an integral boundary of the flow, the boundary condition at the wall must satisfy the similarity requirement as well. For a tunnel with perforated walls the similarity scaling shows that the porosity of the wall should be the same for the tests of two models. This condition is automatically satisfied for the present tunnel with fixed wall porosity. A similarity scaling of the boundary condition at the wall is given in Appendix C.

4.0 EXPERIMENTAL PROGRAMS

4.1 Experimental Methods

The experiments were performed in the NAE 5 ft (1.5 m) × 5 ft (1.5 m) blowndown wind tunnel. The tunnel system and performance are described in detail in Reference 20. For the present experiment, the 5-ft (1.5 m) square transonic section with perforated walls was used. The model was mounted on the supporting sting which could be pitched at the desired angles with the model remaining in the center of the Schlieren window at the transonic downstream position. The high speed Schlieren system was in operation during the tests. A 1-inch (25.4 mm) Task Corporation MK XIV 6-component balance was used for measurements of forces and moments. The balance was precalibrated outside the tunnel before the test. The base pressure of the model was measured by a pressure transducer installed in the cavity of the sting. Static pressure pipes of 1 inch (25.4 mm) diameter were mounted along the center line of the top and the bottom walls respectively for measurements of static pressure distribution near the wall.

Four models were tested in the program: two wing-bodies, WB1 with small wing and WB2 with large wing; and two equivalent bodies of revolution, B1 for zero lift and B2 with lift. The test Mach numbers ranged from 0.8 to 1.1. The Reynolds number in the experiment was fixed at 4×10^6 based on the root chord of 6 inches (152.4 mm). High Reynolds number tests were also performed at 8×10^6 for Mach number of 0.94 for some models to check the Reynolds number effect. During each run, the wing-body model WB1 was pitched continuously from -4° to 10° at a pitch rate 1.887 deg/sec and then followed by three stepping incidences at 0°, 5° and 10° nominally. During the constant incidence steps, enough time was allowed for the static pressure at the upper and lower walls to be scanned. Schlieren photographs of the flow field were taken during the test at a rate of 0.8 sec/frame. For the WB2 model with a larger wing span, the range of incidence was half of that of WB1 and the pitch rate was also reduced accordingly.

Tunnel flow angularity was checked at $M_\infty = 0.8$ by testing the model B1 in the normal and the inverted positions. The flow angularity and the geometric asymmetry of the model were deduced from these tests. The geometric asymmetry of the model and the flow angularity obtained were read in directly to the data reduction program for the correction of the geometric incidence of the model. The sting used in the experiment, unfortunately, could not be rotated automatically by the roll mechanism of the supporting system and the model had to be inverted manually. This was a time-consuming process and therefore the flow condition was checked for one Mach number, $M_\infty = 0.8$ only. The flow angularity was found to be 0.53° and the asymmetry of the model caused a further deviation of 0.25°. Since none of the models had been checked for inaccuracy of machining due to lack of time, the degree of asymmetry might be different between the models. Thus only the flow angle offset was incorporated in the data reduction program and the value of 0.55° was used for all models and Mach numbers in the tests.

Because of uncertainty of the flow angularity at this range of Mach numbers, the axi-symmetrical bodies were also tested in a similar "ramp and step" program with the pitch angle ranged from -3° to 3° and steps at 0.1°, 0.2° and 0.3°, from which the minimum drag was obtained.

Surface flow visualization was applied to a few tests to provide information on boundary layer transition, separation and formation of leading edge vortices.

4.2 Data Reduction

The experimental data were reduced on-line after each run. Some important data such as C_L vs α and C_D vs C_L were plotted after the data had been reduced to coefficient forms. This large amount of data were further analyzed using the computer of the NRC Computation Center and organized in parametric forms suitable for the present studies.

The preliminary results of the wing-body models indicate that the C_L vs α curves do not pass through the origin of the co-ordinates. The axis of symmetry of the C_D vs C_L polars also offset

slightly from the C_L axis. This, as discussed in the previous section, is due to the asymmetry of the model and that the tunnel flow angularity at other Mach numbers may be slightly different for that of $M_\infty = 0.8$ which is used in the data reduction program for flow angularity correction. These effects are corrected for the experimental data and both C_L vs α and C_D vs C_L curves are adjusted to appear as from a symmetric model lining up properly with the tunnel flow. The estimation of the offsetting of the data is given in Appendix D. The data are then presented in terms of $\overline{C}_L$, $\overline{\alpha}$ and C_D in Figures 5 and 6 for the models WB1 and WB2 respectively. The values of these data are listed in Tables 1 and 2 respectively.

The data presented have not been corrected for the wind tunnel wall interference. It has been discussed in Section 3.6 that at transonic speeds, the tunnel wall interference can no longer be treated as a weak correction. Thus the data are presented as obtained with the tunnel walls as an integral part of the flow boundaries. It is desirable, nevertheless, if the effect of the wall constraint can be estimated even in the low Mach number range. In the limit, the subsonic theory may be considered to be applicable asymptotically. The subsonic interference theory shows that the angle of attack and the drag corrections are proportional to the area ratio of the model's maximum cross-section to that of the working section of the tunnel[21]. For the present experiment, the ratio has a value of 0.001 and the corrections due to the wall constraint is thus negligible in the subsonic limit. At transonic speeds the effect of the tunnel constraint will depend on the ratio of the transverse scale $b/\widetilde{\epsilon}$ and the tunnel height and width as discussed.

For the axisymmetric equivalent bodies the drag at zero lift is taken directly from the experimental data and no further processing is needed. The cross-sectional area of the body B1 is identical to the wing-body, the blockage effect is very small at the subsonic flow range and no correction is applied. In the transonic range, the outer flow field is equivalent to that of the wing-body, thus the tunnel flow must be considered as a complete system.

5.0 EXPERIMENTAL RESULTS AND DISCUSSIONS

5.1 Drag at Zero Lift

The experimental results are first checked against the classical area rule. The transonic wave drag is deduced from the total drag by subtracting the viscous drag and the pressure drag which is the total drag before the drag-rise. At small and zero incidence, the drag in subcritical flows is dominated by viscous drag. For the present experiment the drag at Mach number of 0.8 is used as the viscous drag. The transonic drag-rise is shown in Figure 7 presented in the similarity form as defined in Equation (11). The drag parameter is normalized by the maximum cross-sectional area S_c of the model and the transonic similarity parameter K is in terms of slenderness ratio τ_b based on S_c. With the parameters in these forms the data of the wing-bodies and the equivalent bodies can be compared directly. The drag-rise of the wing-body WB2 and the equivalent body B1 are very close through the Mach number range considered. The wing-body WB1 with a wing of smaller aspect ratio but a thicker section gives persistently higher drag than the model WB2. This seems to be contradicting the classical area rule, which works better for wings with small aspect ratios[18,22]. This discrepancy is believed to be caused by stronger shock loss in the near field and shock boundary layer interaction for the WB1 model.

The boundary layer transition on the wing is natural and occurs about one inch (25.4 mm) downstream parallel to the leading edge for both models. This relatively large extent of laminar boundary layer interacts with the wing shock causing flow separation in the wing tip region, can be seen in the flow visualization on the wing surface, Figure 8. The separation appears to be more severe on the WB1 model with a thicker wing. The strong shock wave in the near field of the model WB1 also causes higher drag. Drag due to shock loss is proportional to $[M]^3$ where [ ] denotes the difference of conditions in front and behind the shock and in transonic flows this can be shown to be proportional to $[U]^3$ for small disturbances[23]. Near the wings the local drag due to the shock loss per unit spanwise length can be approximately related as $D_1 \simeq (1.8)^3 D_2$, where the thickness ratio of the two wings is 1.8. Integrating along the span and noting that $b_1 = b_2/1.8$, we have $D_1 = 3.24\, D_2$. Thus in the near field the shock loss of the model WB1 is much higher than that of WB2,

consistent with the observed drag-rise as shown in Figure 7. This confirms further that the area rule works better with thin wings; for example, the excellent correlations obtained by Whitcomb apply for models with wing thickness of 4 percent which generate relatively weak shocks in the near field.

The close correlation of the drag-rise of the wing-body and the equivalent body confirms the equivalence rule at zero lift. The shock structures of the wing-body and the equivalent body are shown in the Schlieren flow visualizations in Figure 9 and indicate the similitude of the outer flow fields. In the near field of the wing-body, the shock is formed near the trailing edge of the wing and is stronger for the model WB1 with a thicker wing than the model WB2. For the equivalent body, the shock is located at the rear part of the bulge and is more oblique near the body surface. The boundary layer does not appear to separate at the rear end of the bulge, nor strong shock-boundary layer interaction is indicated. The shocks on all models change rapidly to axisymmetric normal shocks within a transverse distance of two body diameters, forming closely similar outer flow fields.

The outer flow similarity can also be examined from the pressure distributions along the upper and lower walls. Figure 10 shows the variation of the pressure coefficient along the walls for all three models at Mach number of 0.98. Similarity of the outer flow fields of all three models are observed. The outer flow pressure variations reflect directly the source distribution along the body axis and only weakly retain the rapid variation of the flow quantities near the body. At other Mach numbers, the outer flow similitude has also been observed from the Schlieren flow visualizations and the pressure distributions near the walls. The trend is closely similar to the cases just discussed.

5.2 Lift

The lift vs angles of attack curves for both models have already been presented in Figures 5 and 6. The linear portion of the lift curve before onset of flow separation can be represented by the lift curve slope at zero lift, $\bar{C}_{L_{\alpha_o}}$. In Figure 11, the lift slopes are correlated in the form of the classical transonic similarity law, which applies to the present models with geometric similar wing plan forms and sections. At subsonic speeds both models follow a similar trend with increasing lift slope as Mach number increases but fail to reach the theoretical value of $\pi/2$ at Mach unity. At supersonic speeds, the correlations are less coherent and the lift slopes decrease as Mach number increases. At the low Mach number end, the corresponding incompressible values of $\bar{C}_{L_\alpha}$ and A obtained from applying the linear compressibility transformation follow the existing data for delta wing and the lifting surface theory closely[24]. At Mach number unity, the values follow the transonic correlation in the form $C_{L_\alpha}\ (t/c)^{1/3}$ vs $A(t/c)^{1/3}$ [25]. The model WB1 with smaller aspect ratio is within the linear range (slender body theory), while the model WB2 with larger span is beyond the linear range.

As the flow Mach number approaching unity, the lift slope $C_{L_{\alpha_o}}$ depends strongly on the shock movements at the upper and the lower surface of the wing[26,27]. The large dip at $M_\infty = 0.96$ for the model WB1 is caused by the movement of the lower surface shock towards the trailing edge while the upper surface shock remains nearly stationary at small positive incidence. This increases the total suction at the lower surface and hence reduces the lift. At higher Mach number, both shocks move to the trailing edge and the lift recovers. For the thin wing, the difference of the shock movement is less severe and loss of lift does not occur.

When the angle of attack increases to about the value of the wing thickness, the flow separates from the leading edge and rolls up into a vortex. This can be seen clearly from the surface streamline patterns as shown in the flow visualization pictures Figure 12. For the model WB1, at 5 degree incidence, the leading edge vortex is still weak and lies close to the leading edge. At 10 degree incidence a strong conical vortex is located along a generator of the delta wing well in-board from the leading edge. A similar flow pattern can also be observed over the wing of the model WB2 at incidences about one half of that of WB1. The lift induced by the vortex, however, is less significant than that on the highly slender wings[28,29]. The lift curves do not appear to have appreciable nonlinear lift contributions even at subsonic Mach numbers (see Figs. 5 and 6).

The equivalence rule outlined in Section 2 are based on the solutions of the attached flow[5]. Flows with leading edge separation has been treated by Barnwell[6,7] and the results are closely similar to those given in Reference 5. Thus the equivalence rule in the present form will apply to the complete range of C_L investigated in the experiment.

5.3 Induced Drag

The drag measured in the experiment consists of contributions from the skin friction, pressure forces including those due to shock waves and drag induced by lift. At subcritical conditions, there are no shock waves and the pressure drag is much smaller that the viscous drag. Thus before the transonic drag rise the total drag contains the viscous drag and the lift induced drag only. At zero lift the induced drag is zero and the measured drag can be considered as mainly skin friction drag. The boundary layer flows, however, depend on the incidence and as the Mach number increases, shock boundary layer interaction may also occur, thus the viscous drag will depend on both the flow Mach number and the angle of attack of the model. However, the effect of incidence on the viscous drag, before the onset of separation on the wing surface is known to be small. Thus for the present study the skin friction drag is assumed to be invariant and have the value equivalent to the drag measured at Mach number of 0.8 and zero angle of attack.

The drag induced by lift is well established in the wing theory[25,30]. For a delta wing with small aspect ratio, the slender wing theory gives the induced drag

$$C_{D_i} = \frac{C_L^2}{\pi A} \tag{27}$$

which is the optimized value corresponding to an elliptical loading. For a general planform,

$$C_{D_i} = k \frac{C_L^2}{\pi A} \tag{28}$$

where k is the induced drag factor which depends on the planform shape. The induced drag can also be considered as a component of the normal force in the free-stream direction subtracting the suction force that may exist at the leading edge of the wing. If there is no suction force, the induced drag is simply

$$C_{D_i} = C_L \alpha \tag{29}$$

which is twice as large as that when a full suction force is present, Equation (27). For a general planform, the induced drag falls in between these two extremes and is a function of the lift and the lift curve slope[25]. It is written in a general form as

$$C_{D_i} = \tilde{k} \frac{C_L^2}{C_{L_\alpha}} \tag{30}$$

where $\tilde{k}$ is the induced drag factor.

The drag polars for both models at Mach number 0.8 are replotted in terms $\bar{C}_L^2$ in Figure 13 for both models. The limits for a full suction force and no suction are also shown. The experimental data fall in between these limits. At low lift, the leading edge suction reaches about a half of the full value and decreases steadily as the lift increases. The correlation also shows that $\bar{C}_D$ is not a linear function of $\bar{C}_L^2$. Thus the general relation Equation (30) should be used to correlate the induced drag with lift.

As the Mach number increases the drag due to formation of shock wave appears. For the wing-body configurations there are two shocks formed over the model, one at the end of the nose section and the other at the rear of the wing. From the experimental data of the axisymmetric bodies, it is found that the variation of the nose wave drag with incidence is very small. Thus the increase of drag with incidence is attributed mainly to the wave drag and the induced drag due to lift of the wing. The drag data with the zero lift value C_{D_o} subtracted are plotted in terms $\bar{C}_D \bar{C}_{L_{\bar{\alpha}}}$ against $\bar{C}_L^2$ in Figures 14 and 15 for the two wing body models respectively. Most of the data are successfully correlated by a straight line. At the high lift end, the data deviate from the straight line correlation as the values of C_{L_α} decrease rapidly at high incidences with flow separation occurring on the upper surface of the wing.

5.4 Lift-Depending Wave Drag

The slope of the correlation curve discussed in the preceding section gives the overall lift-depending drag factor which consists of the induced drag due to lift and the lift-depending wave drag[31]. The drag induced by lift is independent of Mach number[24]. Thus the value of $\tilde{k}$ at Mach number of 0.8 before the drag-rise can be taken as the induced drag factor for all cases. The lift-depending wave drag can now be deduced as

$$\bar{C}_{D_w} = (\tilde{k} - \tilde{k}_{0.8}) \frac{\bar{C}_L^2}{\bar{C}_{L_\alpha}} \tag{31}$$

The values of $\tilde{k}$ as a function of Mach number are shown in Figure 16.

The lift-depending wave drag is now presented in terms of the parameters of the equivalence rule. The conditions of equivalence require the doublet and the effective source to be identical at the same transonic similarity parameter K. From Equation (24), the parameter controlling the lift is $\tilde{\epsilon}\tilde{\alpha}_\ell/\tilde{\tau}$ which can be written in terms of the experimental variables as

$$\tilde{\epsilon}\frac{\tilde{\alpha}_\ell}{\tilde{\tau}} = \frac{(\gamma+1)^{1/2}}{2}\frac{c_o}{\ell}\frac{1}{(\tilde{\lambda}\tilde{\tau})^{1/2}}(M_\infty \tilde{\lambda} C_L) \tag{32}$$

For the present experiment, $(\tilde{\lambda}\tilde{\tau})$, c_o/ℓ are identical for both models, thus the lift controlling parameter can be expressed as $M_\infty \tilde{\lambda} C_L$. The drag coefficient is now referenced to the maximal cross-sectional area of the model. The results in terms of these parameters are shown in Figure 17. The abscissa is given in two scales, $M_\infty \tilde{\lambda} C_L$ as in Equation (32) and $\tilde{\epsilon}\tilde{\alpha}_\ell/\tilde{\tau} = \tilde{\sigma}^* \mid \ell n \tilde{\epsilon} \mid^{-1/2}$ as in the original form of the parameter, Equations (3) and (24). The results are presented from Mach number of 0.9 to 1.1. Below 0.9 the wave drag is negligibly small. The values of the transonic similarity parameter K is given beside the Mach number for each case. For most cases, the correlation of the wave drag with the lift parameter is found to be similar for both models. The correlation demonstrates that for the models with the same cross-sectional area but different aspect ratios and thicknesses of the wings, if the lift and the effective cross-sectional area due to lift are the same at a given transonic similarity parameter, then the wave drag due to lift is the same. The equivalence rule with lift is thus established experimentally. For the case of Mach number 0.96, the model WB1 has a much larger drag-rise due to lift than other cases. This is caused by the low value of the lift curve slope at this particular Mach number as discussed in Section 5.2. Thus in order to achieve the same lift condition as defined by the lift parameter, the model has to be at much higher incidence than in the other cases and hence larger drag is obtained.

For the lifting condition with the lift parameter $\epsilon\,\alpha_\ell/\tau$ of 0.2, the equivalent body, B2, with effective area due to lift added to the basic body, B1, was tested in the same Mach number range (see Section 3.5). The drag-rise of the equivalent body and the wing-bodies at the design lift condition are shown in Figure 18 presented in terms of the similarity parameters. The difference in zero lift drag of the wing-bodies as shown in Figure 7 is again reflected in the higher drag-rise for the WB1

model. The drag-rise of the equivalent body B2 is slightly lower than that of the wing-body WB2. This discrepancy is due to the boundary layer separation at the rear of the hump of the equivalent body giving an effective fairing to the body contour, much less abrupt than the physical one. This effective broadening of the hump generates a weaker shock than that which may have formed if there had been no separation and hence a lower drag-rise. The boundary layer separation at the rear of the hump and the reattachment downstream at the aft body can be seen clearly from the surface oil flow visualizations in Figure 19. The rounding off of the wing tips to produce a more gradual change of the body contour as discussed in Section 3.3 does not seem to be adequate in preventing flow separation.

The Schlieren flow visualizations for both wing-body and the equivalent body models at the design lift condition are shown in Figure 20. Since the Schlieren pictures are taken at a fixed time interval during continuous pitching sequence of the test, the lift parameter cannot be matched exactly for both models and the condition shown in the Figures are the ones closest to the design lift condition. The shock patterns over the wings of both wing-body models are closely similar. It should be noted that for the same lift parameter the angle of attack is not the same for the models. The shock pattern over the rear part of the body B2 is more complicated than those of the wing-bodies. It indicates clearly a strong interaction of the shock with the boundary layer separating at the rear of the hump of the body.

The similarity of the far field can be further examined by the static pressure variations near the tunnel walls as in the zero lift cases. The static pressure distirbutions at Mach numbers of 0.94 are shown in Figure 21. The pressure coefficient is now written in the similarity form as defined in Equation (10), so that the data of the equivalent body B2 which has a slightly larger maximal cross-section can be compared in the same scale. Because the pressure scanning was done at predetermined incidences as described in Section 4.1, the lift parameters of two models cannot be matched exactly. The cases shown in the Figures are the closest matches that can be obtained, although the lift parameter has a larger value than the design condition for the equivalent body B2. Taking into consideration the data scattering and the pressure signal being very weak, the data for both models follow the same trend closely. At lifting conditions the upper and the lower wall pressure distributions are no longer the same. At the lower wall a strong compression directly underneath the models can be observed. The pressure distributions for the equivalent body B2 are also plotted in the Figure. Because of the difference in the lift parameter, the data cannot compare quantitatively with the wing-body results. Qualitatively, the data at the upper wall follows the trend of the wing-body data closely, since the lifting wing and the humped body both have the same flow pattern of an expansion followed by a recompression shock. Having a smaller lift parameter, the magnitude of the B2 data is consistently lower than those of the wing-body. The B2 data at the lower wall is closely similar to those of the upper wall because of axial symmetry and do not have a region of compression as generated by a lifting wing.

6.0 CONCLUSIONS

The transonic equivalence rule with lift has been studied experimentally. The experiment has established the similitude of the outer flow fields of two wing-bodies under the conditions defined by the equivalence rule[5]. The two models have the same cross-sectional area distribution but with wings of different aspect ratios and thicknesses. Two equivalent bodies of revolution have also been tested, one corresponding to the zero lift condition and the other with lift. The experimental results are summarized as follows.

The equivalence rule at zero lift works well for the wing-body model with a thin wing with thickness-chord ratio 0.044. For the wing with thickness of 8 percent, the rear field drag caused by the strong shock over the wing gives a higher drag-rise than that of the equivalent body.

The correlations of the lift-depending wave drag and the lift parameter $\epsilon\ \alpha_\ell/\tau$ of two models are closely similar for the tested Mach numbers. Similitude of the outer flow field under the same lift condition defined by the lift parameter is established.

The drag-rise of the equivalent body with lift correlates reasonably well with that of the wing-body at the design lifting condition, though the drag parameter has a slightly lower value throughout the Mach number range. This is caused by the flow separation at the rear of the hump of the body forming an effective contour which reduces the local shock strength.

The experiment therefore verifies the conditions defined by the equivalence rule with lift. It establishes the similitude of the outer flow field at lifting conditions. As in the classical rule of zero lift, the equivalence rule with lift works well for configurations with a thin wing and a gradual variation of the equivalent cross-sectional area which includes the geometric one and the effective area from the axial lift distribution.

7.0 REFERENCES

1. Ashley, H.; Landahl, M. — *Aerodynamics of Wings and Bodies.* Addison-Wesley, Mass. 1965.
2. Oswatitsch, K. — *The Area Rule.* Applied Mech. Reviews, Vol. 10, No. 12, December 1957, pp. 543-545.
3. Whitcomb, R.T. — *A Study of the Zero-Lift Drag-Rise Characteristics of Wing-Body Combinations Near the Speed of Sound.* NACA Report 1273, 1956.
4. Langhans, R.A.; Flechner, S.G. — *Wind Tunnel Investigation at Mach Number from 0.25 to 1.01 of a Transport Configuration Designed to Cruise at Near-Sonic Speeds.* NASA TM X-2622, 1971.
5. Cheng, H.K.; Hafez, M.M. — *Transonic Equivalence Rule: A Nonlinear Problem Involving Lift.* J. Fluid Mech., Vol. 72, Part 1, 1975, pp. 161-187.
6. Barnwell, R.W. — *Analysis of Transonic Flow about Lifting Wing-Body Configurations.* NASA TR R-440, June 1975.
7. Barnwell, R.W. — *Approximate Method for Calculating Transonic Flow About Lifting Wing-Body Configurations.* NASA TR R-452, April 1976.
8. Cheng, H.K. — *Lift Corrections to Transonic Equivalence Rule: Examples.* AIAA Journal, Vol. 15, No. 3, March 1977, pp. 366-373.
9. Sadin, Y. C.-J. — *Qualitative Calculations of Transonic Drag-Rise Characteristics Using the Equivalence Rule.* Proceedings of 11th Congress of the International Council of the Aeronautical Sciences, Vol. II, September 1978, pp. 71-84.
10. Spreiter, J.R. — *On the Application of Transonic Similarity Rules to Wings of Finite Span.* NACA Rept. 1153, 1953.
11. Van der Vooren, J.; Slooff, J.W.; Huizing, G.H.; Van Essen, A. — *Remarks on Similarity on Various Transonic Small Perturbation Equations to Describe Three-Dimensional Transonic Flow; Examples of Computations Using a Fully-Conservative Rotated Difference Scheme.* IN Symposium Transsonicum II, Springer-Verlag, N.Y., 1976.
12. Spreiter, J.R. — *The Aerodynamic Forces on Slender Plane- and Cruciform-Wing and Body Combinations.* NASA Rept. 962, 1950.

13. Baurdoux, H.I.
Boerstoel, J.W.
Symmetrical Transonic Potential Flows Around Quasi-Elliptical Airfoil Sections.
NLR-TR69007U, National Aerospace Laboratory, The Netherlands, December 1968.

14. Kacprzynski, J.J.
Wind Tunnel Tests of a Boerstoel Shockless Symmetrical Airfoil.
NRC, NAE, 5x5 ft Transonic Blowdown Wind Tunnel Project Report 5x5/0061, National Research Council Canada, Ottawa, July 1972.

15. Jones, D.J.
A Description of Several Computer Programs for Modifying the Shape of a Given Airfoil.
NRC, NAE, Lab. Memo. HSA-189, National Research Council Canada, Ottawa, December 1979.

16. Spreiter, J.R.
On the Range of Applicability of the Transonic Area Rule.
NACA TN 3673, 1956.

17. Sheppard, L.M.
Limitations of the Sonic Area Rule.
The Aero. Quart. Vol. 11, August 1960, pp. 248-254.

18. Page, W.A.
Experimental Determination of the Range of Applicability of the Transonic Area Rule for Wings of Triangular Plan Form.
NACA TN 3872, 1956.

19. Goodman, T.R.
The Porous Wall Wind Tunnel: Part II, Interference Effect on a Cylindrical Body in a Two-Dimensional Tunnel at Subsonic Speeds.
Cornell Aeronautical Laboratory Rept. AD-594-A-3, November 1950.

20. Brown, D.
Information of Users of the National Research Council's 5-ftx5-ft Blowdown Wind Tunnel at the National Aeronautical Establishment.
Third Edition. NRC, NAE Lab. Tech. Rept. LTR-HA-6, National Research Council Canada, Ottawa, September 1977.

21. Garner, H.C.
Rogers, E.W.E.
Acum, W.E.A.
Maskell, E.C.
Subsonic Wind Tunnel Wall Corrections.
AGARDograph 109, October 1966.

22. Agnell, N.
Mattsson, R.
Nyberg, S.-E.
Investigation of the Transonic Drag Characteristics for Non-Slender Wing-Body Combinations and their Equivalent Axisymmetric Bodies at Zero Lift.
Proceedings of 11th Congress of the International Council of the Aeronautical Sciences, Vol. II, September 1978, pp. 292-304.

23. Murman, E.M.
Cole, J.D.
Inviscid Drag at Transonic Speeds.
AIAA Paper 74-540, June 1974.

24. Schlichting, H.
Truckenbrodt, E.
Aerodynamics of the Airplane.
McGraw-Hill, New York, Chapters 3 and 4, 1979.

25. Frick, C.W.
The Experimental Aerodynamics of Wings at Transonic and Supersonic Speeds.
IN Aerodynamic Components of Aircraft at High Speeds, Ed. A.F. Donovan and H.R. Lawrence, Princeton Univ. Press, Princeton, New Jersey, 1957.

26. Duncan, W.J.
Thom, A.S.
Young, A.D.
Mechanics of Fluids.
Second Edition, Edward Arnold Publishers Ltd., London, Chapter 9, 1970.

27. Albone, C.M.
Hall, M.G.
Joyce, G.
Numerical Solutions for Transonic Flow Past Wing-Body Combinations.
IN Symposium Transsonicum II, Ed. K. Oswatitsch and D. Rues, Springer-Verlag, New York, 1976, pp. 541-548.

28. Kuchemann, D.
The Aerodynamic Design of Aircraft.
Pergamon Press, Chapter 6, 1978.

29. Squire, L.C.
Jones, J.G.
Stanbrook, A.
An Experimental Investigation of the Characteristics of Some Plane and Cambered 65° Delta Wings at Mach Numbers from 0.7 to 2.0.
R&M 3305, Aeronautical Research Council of Britain, 1963.

30. Jones, R.T.
Cohen, D.
Aerodynamics of Wings at High Speeds.
IN Aerodynamic Components of Aircraft at High Speeds, Ed. A.F. Donovan and H.R. Lawrence, Princeton Univ. Press, Princeton, New Jersey, 1957.

31. Courtney, A.L.
A Collection of Data on the Lift-Dependent Drag of Uncambered Slender Wings at Supersonic Speeds.
CP.757, Aeronautical Research Council, 1964.

TABLE 1

WING SECTIONAL PROFILE

x/c	t/c
0	0.00000
0.05	0.02700
0.10	0.03573
0.20	0.04502
0.30	0.04914
0.40	0.04989
0.50	0.04776
0.60	0.04284
0.70	0.03519
0.80	0.02498
0.90	0.01234
1.00	0.00000

TABLE 2

GEOMETRIES OF THE MODELS

	MODEL WB1	MODEL WB2
body length	ℓ_1 = 17.5 in. (444.5 mm)	ℓ_2 = 17.5 in. (444.5 mm)
body radius	r_1 = 0.875 in. (22.23 mm)	r_2 = 0.875 in. (22.23 mm)
root chord	c_o = 6 in. (152.4 mm)	c_o = 6 in. (152.4 mm)
semi-span	b_1 = 4.0437 in. (102.71 mm)	b_2 = 7.2856 in. (185.05 mm)
wing thickness	t_1/c = 0.8	t_2/c = 0.4444
aspect ratio	A = 2.60	A = 4.69
	$\tilde{\lambda}_1$ = 0.231	$\tilde{\lambda}_2$ = 0.416
	$\tilde{\tau}_1$ = 0.0516	$\tilde{\tau}_2$ = 0.02865

TABLE 3

EFFECTIVE AND GEOMETRIC CROSS-SECTIONAL AREAS AND RADII OF THE EQUIVALENT BODIES OF REVOLUTION

$x - x_o/c_o$	S_c	S_{Lift}	S_e	r_c (in)	r_e (in)
0.00	0.6632	0.0000	0.6632	0.8750	0.8750
0.50	0.6632	0.0012	0.6644	0.8750	0.8758
0.10	0.6632	0.0043	0.6675	0.8750	0.8778
0.15	0.6728	0.0091	0.6819	0.8836	0.8872
0.20	0.7020	0.0155	0.7175	0.9026	0.9101
0.25	0.7369	0.0234	0.7603	0.9254	0.9369
0.30	0.7764	0.0328	0.8092	0.9492	0.9665
0.35	0.8161	0.0436	0.8597	0.9732	0.9962
0.40	0.8564	0.0558	0.9122	0.9968	1.0262
0.45	0.8937	0.0693	0.9630	1.0184	1.0544
0.50	0.9287	0.0841	1.0128	1.0380	1.0813
0.55	0.9578	0.1001	1.0579	1.0542	1.1051
0.60	0.9813	0.1174	1.0987	1.0672	1.1262
0.65	0.9956	0.1359	1.1315	1.0748	1.1429
0.70	1.0000	0.1556	1.1556	1.0774	1.1550
0.75	0.9917	0.1765	1.1682	1.0728	1.1613
0.80	0.9685	0.1985	1.1670	1.0600	1.1607
0.85	0.9262	0.2217	1.1479	1.0368	1.1512
0.90	0.8621	0.2460	1.1081	1.0002	1.1310
0.95	0.7704	0.1570	0.9274	0.9456	1.0347
1.00	0.6632	0.0471	0.7283	0.8750	0.9055

TABLE 4

AERODYNAMIC COEFFICIENTS OF WING-BODY MODEL WB1

MACH NO.=0.801 M=30
RE/FT(M) =7.95

ALPHAB	CLB	CD
-4.6104	-0.2356	0.0233
-4.0185	-0.2085	0.0201
-3.4654	-0.1835	0.0179
-2.9417	-0.1567	0.0158
-2.4310	-0.1128	0.0142
-1.9065	-0.1043	0.0128
-1.3268	-0.0546	0.0119
-0.8158	-0.0515	0.0115
-0.2856	-0.0101	0.0111
0.2530	0.0129	0.0112
0.7681	0.0211	0.0115
1.3105	0.0625	0.0121
1.8618	0.0948	0.0130
2.3973	0.1193	0.0138
2.9331	0.1451	0.0155
3.4606	0.1699	0.0168
4.0149	0.2086	0.0194
4.5427	0.2276	0.0219
5.0689	0.2547	0.0249
5.5998	0.2788	0.0284
6.1313	0.3027	0.0323
6.6643	0.3290	0.0374
7.2439	0.3725	0.0447
7.7631	0.3999	0.0512
8.2931	0.4168	0.0571
8.8227	0.4372	0.0642
9.3531	0.4618	0.0724
9.8704	0.4757	0.0792
10.4122	0.5051	0.0890
10.5583	0.5146	0.0921

MACH NO.=0.874 M=30
RE/FT(M) =8.01

ALPHAB	CLB	CD
-4.7085	-0.2613	0.0267
-4.1057	-0.2224	0.0220
-3.5847	-0.1927	0.0193
-3.0426	-0.1700	0.0171
-2.5217	-0.1300	0.0149
-1.9624	-0.1054	0.0132
-1.4103	-0.0812	0.0121
-0.8596	-0.0355	0.0114
-0.3464	-0.0195	0.0114
0.1917	0.0051	0.0113
0.7400	0.0387	0.0116
1.2924	0.0750	0.0121
1.8029	0.0887	0.0130
2.3587	0.1218	0.0141
2.9072	0.1641	0.0160
3.4264	0.1739	0.0176
3.9718	0.2090	0.0204
4.5243	0.2433	0.0239
5.0584	0.2698	0.0278
5.6022	0.3002	0.0322
6.1417	0.3262	0.0366
6.6825	0.3569	0.0429
7.2457	0.3944	0.0507
7.7668	0.4111	0.0565
8.2946	0.4233	0.0622
8.8211	0.4499	0.0706
9.3524	0.4662	0.0775
9.8703	0.4868	0.0859
10.4186	0.5156	0.0962
10.5616	0.5199	0.0982

MACH NO.=0.849 M=30
RE/FT(M) =8.02

ALPHAB	CLB	CD
-4.7101	-0.2552	0.0251
-4.1226	-0.2219	0.0214
-3.5911	-0.1858	0.0184
-3.0505	-0.1678	0.0162
-2.5319	-0.1344	0.0148
-1.9886	-0.1065	0.0133
-1.4170	-0.0691	0.0119
-0.9058	-0.0513	0.0116
-0.3720	-0.0193	0.0114
0.1847	0.0088	0.0114
0.7111	0.0373	0.0116
1.2487	0.0644	0.0120
1.7882	0.0940	0.0129
2.3289	0.1196	0.0139
2.8631	0.1484	0.0156
3.4377	0.1941	0.0177
3.9487	0.2082	0.0198
4.4900	0.2356	0.0226
5.0172	0.2617	0.0261
5.5771	0.3072	0.0313
6.1161	0.3263	0.0356
6.6363	0.3482	0.0407
7.1523	0.3661	0.0457
7.6930	0.3913	0.0524
8.2477	0.4149	0.0594
8.7711	0.4418	0.0672
9.3033	0.4586	0.0747
9.8256	0.4807	0.0833
10.3768	0.5085	0.0935
10.5367	0.5161	0.0963

MACH NO.=0.899 M=30
RE/FT(M) =8.04

ALPHAB	CLB	CD
-4.7134	-0.2644	0.0282
-4.1301	-0.2331	0.0238
-3.5636	-0.2027	0.0206
-3.0473	-0.1822	0.0179
-2.5393	-0.1457	0.0157
-1.9415	-0.1043	0.0136
-1.4270	-0.0772	0.0126
-0.8999	-0.0541	0.0120
-0.3309	-0.0181	0.0116
0.2017	0.0153	0.0116
0.7468	0.0385	0.0119
1.2757	0.0680	0.0123
1.8146	0.0994	0.0132
2.3692	0.1308	0.0149
2.9085	0.1621	0.0167
3.4717	0.2055	0.0195
3.9947	0.2224	0.0221
4.5424	0.2571	0.0261
5.0853	0.2895	0.0305
5.5989	0.2988	0.0339
6.1788	0.3448	0.0407
6.7241	0.3731	0.0468
7.2519	0.3982	0.0532
7.7521	0.4059	0.0580
8.3058	0.4298	0.0655
8.8466	0.4547	0.0737
9.3585	0.4751	0.0814
9.8879	0.4964	0.0897
10.4518	0.5257	0.1005
10.5913	0.5307	0.1028

TABLE 4

AERODYNAMIC COEFFICIENTS OF WING-BODY MODEL WB1 (Cont'd)

MACH NO.=0.918 M=30
RE/FT(M)=8.01

ALPHAB	CLB	CD
-4.6644	-0.2665	0.0307
-4.0792	-0.2253	0.0257
-3.5358	-0.2007	0.0221
-2.9895	-0.1734	0.0192
-2.5010	-0.1522	0.0171
-1.9085	-0.1274	0.0145
-1.3710	-0.0851	0.0131
-0.8293	-0.0407	0.0126
-0.2898	-0.0120	0.0121
0.2522	0.0113	0.0122
0.8000	0.0480	0.0124
1.3400	0.0779	0.0132
1.8836	0.1120	0.0143
2.4380	0.1430	0.0162
2.9620	0.1675	0.0183
3.5355	0.2057	0.0215
4.0616	0.2348	0.0249
4.6007	0.2585	0.0288
5.1449	0.2902	0.0332
5.6954	0.3249	0.0389
6.2207	0.3468	0.0435
6.7544	0.3682	0.0492
7.3026	0.3930	0.0553
7.8276	0.4178	0.0623
8.3623	0.4399	0.0694
8.8987	0.4616	0.0770
9.4238	0.4788	0.0843
9.9583	0.5031	0.0933
10.4949	0.5272	0.1024
10.6582	0.5361	0.1058

MACH NO.=0.960 M=30
RE/FT(M)=8.08

ALPHAB	CLB	CD
-4.6517	-0.2409	0.0388
-4.0592	-0.2062	0.0344
-3.5401	-0.1819	0.0311
-2.9910	-0.1554	0.0284
-2.4760	-0.1316	0.0262
-1.9233	-0.1064	0.0247
-1.3999	-0.0839	0.0233
-0.8339	-0.0398	0.0223
-0.3112	-0.0214	0.0219
0.2505	0.0159	0.0221
0.7792	0.0481	0.0223
1.3491	0.0883	0.0234
1.8757	0.1083	0.0242
2.4079	0.1304	0.0259
2.9412	0.1495	0.0280
3.4913	0.1763	0.0304
4.0188	0.2017	0.0333
4.5804	0.2377	0.0372
5.1182	0.2673	0.0415
5.6730	0.3065	0.0472
6.2033	0.3325	0.0521
6.7596	0.3705	0.0587
7.3029	0.4081	0.0659
7.8601	0.4368	0.0729
8.3655	0.4539	0.0791
8.9419	0.4943	0.0893
9.4788	0.5206	0.0980
10.0127	0.5442	0.1067
10.5505	0.5661	0.1157
10.7191	0.5791	0.1198

MACH NO.=0.939 M=30
RE/FT(M)=8.00

ALPHAB	CLB	CD
-4.7017	-0.2546	0.0340
-4.1501	-0.2353	0.0301
-3.5819	-0.2042	0.0258
-3.0432	-0.1789	0.0228
-2.5494	-0.1557	0.0206
-1.9763	-0.1261	0.0181
-1.4374	-0.0884	0.0161
-0.9122	-0.0618	0.0152
-0.3399	-0.0166	0.0145
0.2255	0.0319	0.0145
0.7376	0.0505	0.0149
1.2798	0.0834	0.0159
1.8323	0.1164	0.0173
2.3699	0.1441	0.0192
2.9193	0.1709	0.0217
3.4676	0.1943	0.0245
3.9979	0.2258	0.0282
4.5379	0.2530	0.0320
5.0853	0.2869	0.0368
5.6260	0.3195	0.0421
6.1838	0.3470	0.0477
6.7215	0.3845	0.0546
7.2565	0.4006	0.0599
7.7989	0.4240	0.0666
8.3312	0.4455	0.0734
8.8738	0.4772	0.0829
9.3957	0.4877	0.0890
9.9190	0.5166	0.0983
10.4699	0.5382	0.1076
10.6312	0.5446	0.1104

MACH NO.=0.981 M=30
RE/FT(M)=8.02

ALPHAB	CLB	CD
-4.7614	-0.2894	0.0515
-4.2002	-0.2545	0.0470
-3.6183	-0.2046	0.0422
-3.0845	-0.1911	0.0402
-2.5600	-0.1552	0.0378
-1.9929	-0.1183	0.0355
-1.4573	-0.0909	0.0342
-0.9136	-0.0544	0.0332
-0.3567	-0.0216	0.0326
0.1773	0.0080	0.0324
0.7598	0.0560	0.0331
1.2749	0.0740	0.0340
1.8253	0.1077	0.0350
2.3751	0.1449	0.0370
2.9109	0.1734	0.0391
3.4546	0.2054	0.0415
4.0059	0.2436	0.0450
4.5353	0.2611	0.0477
5.1209	0.3073	0.0528
5.6646	0.3449	0.0579
6.1920	0.3677	0.0626
6.7509	0.3991	0.0688
7.2777	0.4293	0.0749
7.8507	0.4611	0.0827
8.3630	0.4874	0.0897
8.9338	0.5176	0.0986
9.4575	0.5358	0.1060
9.9990	0.5728	0.1162
10.5519	0.6089	0.1275
10.6699	0.6116	0.1291

TABLE 4

AERODYNAMIC COEFFICIENTS OF WING-BODY MODEL WB1 (Cont'd)

MACH NO.=0.999 M=30
RE/FT(M)=7.96

ALPHAB	CLB	CD
-4.8323	-0.3070	0.0548
-4.2140	-0.2680	0.0499
-3.6644	-0.2237	0.0454
-3.1390	-0.1941	0.0424
-2.6022	-0.1566	0.0399
-2.0332	-0.1251	0.0378
-1.4935	-0.1013	0.0360
-0.9692	-0.0654	0.0351
-0.3837	-0.0084	0.0345
0.1587	0.0101	0.0344
0.6971	0.0472	0.0350
1.2552	0.0774	0.0357
1.7885	0.1151	0.0369
2.3120	0.1330	0.0384
2.8746	0.1719	0.0407
3.4166	0.2028	0.0431
4.0029	0.2502	0.0472
4.5290	0.2761	0.0505
5.0650	0.3032	0.0546
5.6275	0.3458	0.0599
6.1656	0.3706	0.0651
6.7107	0.4027	0.0707
7.2506	0.4249	0.0765
7.7930	0.4571	0.0842
8.3412	0.4871	0.0919
8.8710	0.5143	0.0998
9.4363	0.5469	0.1093
9.9823	0.5750	0.1187
10.5087	0.6002	0.1281
10.6730	0.6111	0.1315

MACH NO.=1.051 M=30
RE/FT(M)=8.01

ALPHAB	CLB	CD
-4.7200	-0.2755	0.0600
-4.1507	-0.2494	0.0560
-3.6275	-0.2201	0.0526
-3.0464	-0.1889	0.0495
-2.5324	-0.1503	0.0470
-1.9589	-0.1081	0.0446
-1.4072	-0.0739	0.0431
-0.8830	-0.0513	0.0422
-0.3355	-0.0214	0.0418
0.2136	0.0061	0.0418
0.7604	0.0387	0.0423
1.3097	0.0741	0.0431
1.8708	0.1137	0.0445
2.4095	0.1393	0.0463
2.9289	0.1641	0.0482
3.4798	0.2037	0.0512
4.0539	0.2394	0.0546
4.5794	0.2597	0.0579
5.1330	0.2963	0.0623
5.6894	0.3366	0.0679
6.2508	0.3760	0.0740
6.7899	0.4012	0.0792
7.3267	0.4336	0.0863
7.8701	0.4563	0.0928
8.4152	0.4823	0.1002
8.9697	0.5156	0.1092
9.5042	0.5454	0.1183
10.0337	0.5638	0.1265
10.6077	0.5992	0.1380
10.7465	0.6023	0.1401

MACH NO.=1.026 M=30
RE/FT(M)=7.99

ALPHAB	CLB	CD
-4.7905	-0.2935	0.0585
-4.1991	-0.2571	0.0537
-3.6454	-0.2139	0.0495
-3.0994	-0.1868	0.0467
-2.5834	-0.1589	0.0446
-2.0126	-0.1266	0.0424
-1.4646	-0.0913	0.0407
-0.9210	-0.0527	0.0395
-0.3598	-0.0218	0.0390
0.1860	0.0170	0.0390
0.7286	0.0473	0.0395
1.2734	0.0809	0.0402
1.8288	0.1139	0.0417
2.3594	0.1356	0.0433
2.9060	0.1689	0.0455
3.4693	0.2154	0.0487
4.0216	0.2482	0.0518
4.5726	0.2812	0.0559
5.0889	0.3049	0.0597
5.6549	0.3372	0.0647
6.1990	0.3728	0.0703
6.7454	0.4066	0.0765
7.2902	0.4350	0.0829
7.8320	0.4617	0.0897
8.3771	0.4909	0.0973
8.9086	0.5096	0.1042
9.4636	0.5445	0.1139
10.0169	0.5734	0.1233
10.5501	0.5968	0.1323
10.7117	0.6028	0.1349

MACH NO.=1.098 M=30
RE/FT(M)=7.97

ALPHAB	CLB	CD
-4.8133	-0.2806	0.0587
-4.2113	-0.2451	0.0538
-3.6942	-0.2232	0.0509
-3.1322	-0.1848	0.0473
-2.6095	-0.1528	0.0450
-2.0467	-0.1158	0.0423
-1.5027	-0.0897	0.0409
-0.9698	-0.0524	0.0397
-0.4108	-0.0177	0.0392
0.1243	0.0013	0.0391
0.6755	0.0363	0.0396
1.2198	0.0704	0.0404
1.7658	0.1044	0.0417
2.3161	0.1317	0.0435
2.8603	0.1664	0.0458
3.4185	0.1993	0.0486
3.9578	0.2260	0.0516
4.5072	0.2652	0.0556
5.0616	0.2988	0.0604
5.6048	0.3307	0.0652
6.1409	0.3559	0.0703
6.7128	0.3957	0.0772
7.2439	0.4210	0.0831
7.8092	0.4529	0.0906
8.3348	0.4758	0.0975
8.8778	0.4995	0.1051
9.4152	0.5215	0.1129
9.9788	0.5548	0.1232
10.5075	0.5837	0.1331
10.6944	0.5945	0.1369

TABLE 4

AERODYNAMIC COEFFICIENTS OF WING-BODY MODEL WB1 (Cont'd)

MACH NO.=0.956 M=30
RE/FT(M)=16.14

ALPHAB	CL B	CD
-6.2987	-0.3417	0.0537
-5.6450	-0.3040	0.0467
-5.0213	-0.2593	0.0399
-4.4442	-0.2341	0.0357
-3.8784	-0.1971	0.0313
-3.3123	-0.1846	0.0287
-2.7130	-0.1477	0.0255
-2.0709	-0.1015	0.0230
-1.5361	-0.0896	0.0213
-0.9039	-0.0540	0.0205
-0.3069	-0.0151	0.0204
0.3086	0.0257	0.0200
0.8678	0.0505	0.0207
1.4642	0.0822	0.0215
2.0622	0.1088	0.0229
2.6210	0.1317	0.0245
3.2359	0.1702	0.0279
3.8334	0.2012	0.0311
4.4232	0.2295	0.0348
5.0438	0.2771	0.0404
5.6326	0.3105	0.0459
6.2771	0.3555	0.0536
6.8431	0.3846	0.0604
7.4560	0.4184	0.0683
8.0534	0.4532	0.0772
8.6366	0.4788	0.0857
9.2270	0.5081	0.0951
9.7903	0.5347	0.1044
10.3826	0.5642	0.1154
10.8394	0.5958	0.1260

TABLE 5

AERODYNAMIC COEFFICIENTS OF WING-BODY MODEL WB2

MACH NO.=0.918 M=29
RE/FT(M)=8.04

ALPHAB	CLB	CD
-2.8951	-0.2806	0.0197
-2.5410	-0.2414	0.0166
-2.2419	-0.2285	0.0152
-1.9684	-0.2138	0.0140
-1.6442	-0.1645	0.0118
-1.2439	-0.1207	0.0102
-0.9284	-0.0865	0.0093
-0.6144	-0.0575	0.0088
-0.2973	-0.0330	0.0086
0.0368	0.0024	0.0085
0.3929	0.0386	0.0087
0.6986	0.0649	0.0089
1.0368	0.1017	0.0096
1.3486	0.1259	0.0104
1.7147	0.1727	0.0120
2.0449	0.2062	0.0136
2.3519	0.2328	0.0152
2.6960	0.2738	0.0177
3.0755	0.3269	0.0216
3.3897	0.3539	0.0243
3.6921	0.3742	0.0268
4.0467	0.4171	0.0315
4.3705	0.4518	0.0359
4.6778	0.4753	0.0398
5.0019	0.5085	0.0449
5.3080	0.5319	0.0492
5.6396	0.5644	0.0550
5.9633	0.5928	0.0605
6.0917	0.5924	0.0620

MACH NO.=0.959 M=28
RE/FT(M)=7.98

ALPHAB	CLB	CD
-3.0072	-0.3173	0.0279
-2.6354	-0.2743	0.0238
-2.2339	-0.2208	0.0201
-1.9581	-0.2020	0.0186
-1.6434	-0.1683	0.0167
-1.3195	-0.1460	0.0152
-1.0408	-0.1331	0.0143
-0.6692	-0.0754	0.0131
-0.3095	-0.0269	0.0124
0.0410	0.0135	0.0123
0.3556	0.0457	0.0124
0.6765	0.0752	0.0129
1.0335	0.1191	0.0140
1.3511	0.1489	0.0154
1.6800	0.1774	0.0169
2.0048	0.2055	0.0188
2.3496	0.2488	0.0214
2.6734	0.2784	0.0238
3.0016	0.3145	0.0270
3.3645	0.3569	0.0312
3.6761	0.3846	0.0346
4.0025	0.4122	0.0382
4.3033	0.4376	0.0421
4.6337	0.4695	0.0466
4.9734	0.5062	0.0522
5.2764	0.5260	0.0563
5.5916	0.5556	0.0617
5.8656	0.5639	0.0650

MACH NO.=0.938 M=29
RE/FT(M)=7.99

ALPHAB	CLB	CD
-3.0939	-0.3608	0.0272
-2.7243	-0.3219	0.0230
-2.3466	-0.2726	0.0193
-1.9492	-0.2086	0.0156
-1.6936	-0.1879	0.0141
-1.3451	-0.1554	0.0124
-1.0140	-0.1216	0.0110
-0.6579	-0.0711	0.0098
-0.3352	-0.0461	0.0094
0.0409	0.0090	0.0092
0.3833	0.0480	0.0094
0.6980	0.0766	0.0100
1.0875	0.1307	0.0112
1.3933	0.1566	0.0125
1.7380	0.1968	0.0146
2.0756	0.2335	0.0167
2.4265	0.2770	0.0196
2.6907	0.2873	0.0212
3.0578	0.3356	0.0251
3.3711	0.3592	0.0279
3.6462	0.3702	0.0301
4.0592	0.4380	0.0368
4.3782	0.4676	0.0409
4.7014	0.4976	0.0458
5.0102	0.5242	0.0503
5.3396	0.5559	0.0558
5.6201	0.5656	0.0593
5.9804	0.6107	0.0671
6.1159	0.6140	0.0689

MACH NO.=0.979 M=28
RE/FT(M)=8.00

ALPHAB	CLB	CD
-2.9481	-0.2704	0.0295
-2.6123	-0.2399	0.0270
-2.3042	-0.2224	0.0254
-1.9852	-0.1939	0.0234
-1.6799	-0.1613	0.0217
-1.3774	-0.1442	0.0205
-1.0019	-0.0956	0.0190
-0.6663	-0.0519	0.0181
-0.3520	-0.0328	0.0177
-0.0459	-0.0069	0.0176
0.2677	0.0171	0.0178
0.6078	0.0559	0.0181
0.9300	0.0844	0.0187
1.2736	0.1208	0.0199
1.6395	0.1741	0.0219
1.9537	0.1937	0.0231
2.2666	0.2211	0.0250
2.6106	0.2587	0.0273
2.8971	0.2798	0.0291
3.2288	0.3107	0.0319
3.5754	0.3496	0.0356
3.8902	0.3749	0.0387
4.1904	0.3965	0.0420
4.5819	0.4514	0.0480
4.8364	0.4588	0.0500
5.2066	0.5055	0.0565
5.5023	0.5254	0.0607
5.8666	0.5705	0.0677

TABLE 5

AERODYNAMIC COEFFICIENTS OF WING-BODY MODEL WB2 (Cont'd)

MACH NO.=0.801 M=28
RE/FT(M)=8.02

ALPHAB	CLB	CD
-2.7220	-0.1992	0.0133
-2.4110	-0.1757	0.0120
-2.0509	-0.1456	0.0109
-1.8322	-0.1425	0.0108
-1.5134	-0.1110	0.0097
-1.2215	-0.1005	0.0093
-0.8996	-0.0690	0.0086
-0.6309	-0.0523	0.0083
-0.3139	-0.0284	0.0080
0.0055	-0.0018	0.0080
0.2794	0.0130	0.0080
0.6122	0.0486	0.0084
0.9046	0.0652	0.0089
1.2448	0.0986	0.0094
1.5685	0.1388	0.0102
1.8532	0.1487	0.0105
2.1657	0.1750	0.0117
2.4401	0.1878	0.0124
2.7642	0.2191	0.0139
3.0664	0.2435	0.0155
3.3756	0.2656	0.0174
3.6576	0.2828	0.0189
4.0060	0.3210	0.0222
4.2884	0.3366	0.0244
4.6144	0.3699	0.0280
4.8972	0.3790	0.0300
5.1640	0.3874	0.0324
5.4770	0.4286	0.0378

MACH NO.=0.874 M=28
RE/FT(M)=7.99

ALPHAB	CLB	CD
-2.7771	-0.2481	0.0152
-2.4838	-0.2371	0.0143
-2.0953	-0.1854	0.0119
-1.7659	-0.1462	0.0106
-1.4897	-0.1281	0.0102
-1.1157	-0.0844	0.0090
-0.8568	-0.0772	0.0088
-0.5097	-0.0361	0.0082
-0.2036	-0.0169	0.0081
0.1278	0.0174	0.0080
0.4380	0.0395	0.0083
0.7328	0.0621	0.0087
1.0143	0.0737	0.0090
1.3471	0.1056	0.0097
1.6723	0.1336	0.0102
1.9676	0.1521	0.0107
2.3537	0.2100	0.0130
2.6534	0.2296	0.0143
2.9764	0.2606	0.0162
3.2988	0.2894	0.0183
3.6310	0.3260	0.0212
3.9642	0.3546	0.0239
4.2632	0.3744	0.0268
4.5873	0.4050	0.0309
4.8544	0.4127	0.0334
5.1653	0.4353	0.0369
5.4405	0.4455	0.0394
5.7396	0.4793	0.0447

MACH NO.=0.849 M=28
RE/FT(M)=8.03

ALPHAB	CLB	CD
-2.7040	-0.2375	0.0152
-2.3363	-0.1899	0.0124
-1.9861	-0.1585	0.0115
-1.7643	-0.1543	0.0109
-1.4246	-0.1179	0.0098
-1.0979	-0.0889	0.0089
-0.7502	-0.0440	0.0080
-0.5022	-0.0442	0.0081
-0.1540	-0.0126	0.0078
0.1237	0.0098	0.0078
0.4335	0.0281	0.0080
0.7530	0.0607	0.0084
1.0772	0.0845	0.0090
1.3626	0.1030	0.0096
1.6892	0.1369	0.0103
2.0129	0.1644	0.0111
2.3093	0.1857	0.0122
2.6085	0.2082	0.0134
2.9436	0.2438	0.0151
3.2281	0.2512	0.0164
3.5711	0.2929	0.0186
3.8549	0.3093	0.0206
4.2106	0.3513	0.0244
4.5250	0.3720	0.0270
4.8442	0.4039	0.0307
5.1193	0.4125	0.0330
5.4253	0.4367	0.0370
5.6431	0.4404	0.0390

MACH NO.=0.899 M=29
RE/FT(M)=8.01

ALPHAB	CLB	CD
-2.8991	-0.2744	0.0181
-2.5154	-0.2183	0.0145
-2.1785	-0.1981	0.0128
-1.8615	-0.1674	0.0115
-1.5688	-0.1358	0.0105
-1.2745	-0.1202	0.0097
-0.9317	-0.0870	0.0089
-0.6224	-0.0563	0.0085
-0.2906	-0.0258	0.0082
0.0611	0.0103	0.0081
0.3578	0.0349	0.0082
0.6900	0.0649	0.0086
0.9867	0.0839	0.0090
1.2855	0.1020	0.0095
1.6465	0.1495	0.0108
1.9698	0.1834	0.0120
2.3044	0.2142	0.0134
2.6778	0.2659	0.0159
2.9659	0.2830	0.0176
3.2607	0.3012	0.0193
3.5896	0.3298	0.0220
3.9470	0.3776	0.0263
4.2565	0.4026	0.0295
4.5637	0.4222	0.0328
4.8670	0.4447	0.0366
5.1914	0.4723	0.0411
5.5022	0.4962	0.0456
5.7810	0.5049	0.0489
5.9127	0.5037	0.0502

TABLE 5

AERODYNAMIC COEFFICIENTS OF WING-BODY MODEL WB2 (Cont'd)

MACH NO.=0.998 M=28
RE/FT(M)=7.99

ALPHAB	CLB	CD
-2.7925	-0.2530	0.0293
-2.3897	-0.2044	0.0260
-2.1122	-0.1967	0.0250
-1.8252	-0.1772	0.0238
-1.5064	-0.1384	0.0220
-1.1508	-0.1030	0.0207
-0.8326	-0.0774	0.0200
-0.5540	-0.0563	0.0195
-0.1641	-0.0053	0.0190
0.1395	0.0165	0.0191
0.4726	0.0498	0.0193
0.7489	0.0658	0.0197
1.0916	0.0960	0.0205
1.4029	0.1242	0.0214
1.7240	0.1506	0.0227
2.0521	0.1838	0.0244
2.3890	0.2162	0.0260
2.7154	0.2520	0.0283
3.0569	0.2848	0.0310
3.3908	0.3197	0.0340
3.6967	0.3412	0.0366
3.9683	0.3558	0.0389
4.3553	0.4085	0.0443
4.6437	0.4220	0.0470
4.9568	0.4475	0.0510
5.3213	0.4965	0.0573
5.6197	0.5196	0.0616
5.9651	0.5535	0.0675

MACH NO.=1.050 M=28
RE/FT(M)=7.96

ALPHAB	CLB	CD
-2.8654	-0.2631	0.0341
-2.4941	-0.2217	0.0311
-2.1665	-0.1899	0.0289
-1.8327	-0.1554	0.0270
-1.5649	-0.1392	0.0260
-1.1715	-0.0936	0.0243
-0.9047	-0.0827	0.0239
-0.6081	-0.0583	0.0234
-0.2715	-0.0274	0.0231
0.0267	-0.0078	0.0231
0.4012	0.0362	0.0232
0.7164	0.0682	0.0236
1.0652	0.1002	0.0243
1.3810	0.1278	0.0253
1.6865	0.1499	0.0266
1.9845	0.1702	0.0278
2.3335	0.2062	0.0297
2.6715	0.2449	0.0321
2.9863	0.2690	0.0341
3.3295	0.3084	0.0377
3.6379	0.3300	0.0400
3.9409	0.3508	0.0426
4.2854	0.3856	0.0465
4.5949	0.4114	0.0501
4.8978	0.4324	0.0536
5.2034	0.4522	0.0574
5.5497	0.4929	0.0632
5.8688	0.5192	0.0682

MACH NO.=1.025 M=28
RE/FT(M)=8.02

ALPHAB	CLB	CD
-3.0360	-0.2707	0.0332
-2.7145	-0.2532	0.0313
-2.3560	-0.2075	0.0283
-2.0529	-0.1869	0.0270
-1.7548	-0.1558	0.0253
-1.4215	-0.1337	0.0240
-1.1059	-0.1047	0.0230
-0.7217	-0.0472	0.0217
-0.4318	-0.0320	0.0215
-0.1565	-0.0244	0.0215
0.1912	0.0172	0.0215
0.4933	0.0408	0.0217
0.8609	0.0822	0.0223
1.1689	0.1048	0.0230
1.4703	0.1312	0.0240
1.8088	0.1602	0.0254
2.1231	0.1859	0.0268
2.4473	0.2194	0.0287
2.7780	0.2489	0.0308
3.1091	0.2840	0.0337
3.4569	0.3237	0.0372
3.7992	0.3602	0.0406
4.0944	0.3786	0.0434
4.4568	0.4253	0.0486
4.7761	0.4501	0.0522
5.0975	0.4782	0.0565
5.3961	0.4960	0.0602
5.7332	0.5383	0.0666

MACH NO.=1.098 M=28
RE/FT(M)=7.99

ALPHAB	CLB	CD
-2.9786	-0.2515	0.0328
-2.6985	-0.2465	0.0318
-2.2520	-0.1832	0.0277
-2.0000	-0.1679	0.0265
-1.7252	-0.1487	0.0253
-1.3812	-0.1193	0.0239
-1.0241	-0.0810	0.0226
-0.7308	-0.0595	0.0220
-0.4155	-0.0373	0.0217
-0.0922	-0.0063	0.0214
0.2280	0.0199	0.0216
0.5476	0.0472	0.0218
0.8512	0.0719	0.0223
1.1540	0.0905	0.0230
1.4880	0.1210	0.0241
1.8284	0.1557	0.0256
2.1708	0.1924	0.0276
2.4859	0.2176	0.0292
2.7831	0.2350	0.0308
3.1184	0.2677	0.0335
3.4534	0.3017	0.0367
3.7679	0.3246	0.0394
4.0864	0.3541	0.0431
4.4599	0.3988	0.0481
4.7396	0.4130	0.0509
5.0614	0.4403	0.0551
5.3990	0.4752	0.0603
5.6591	0.4879	0.0635

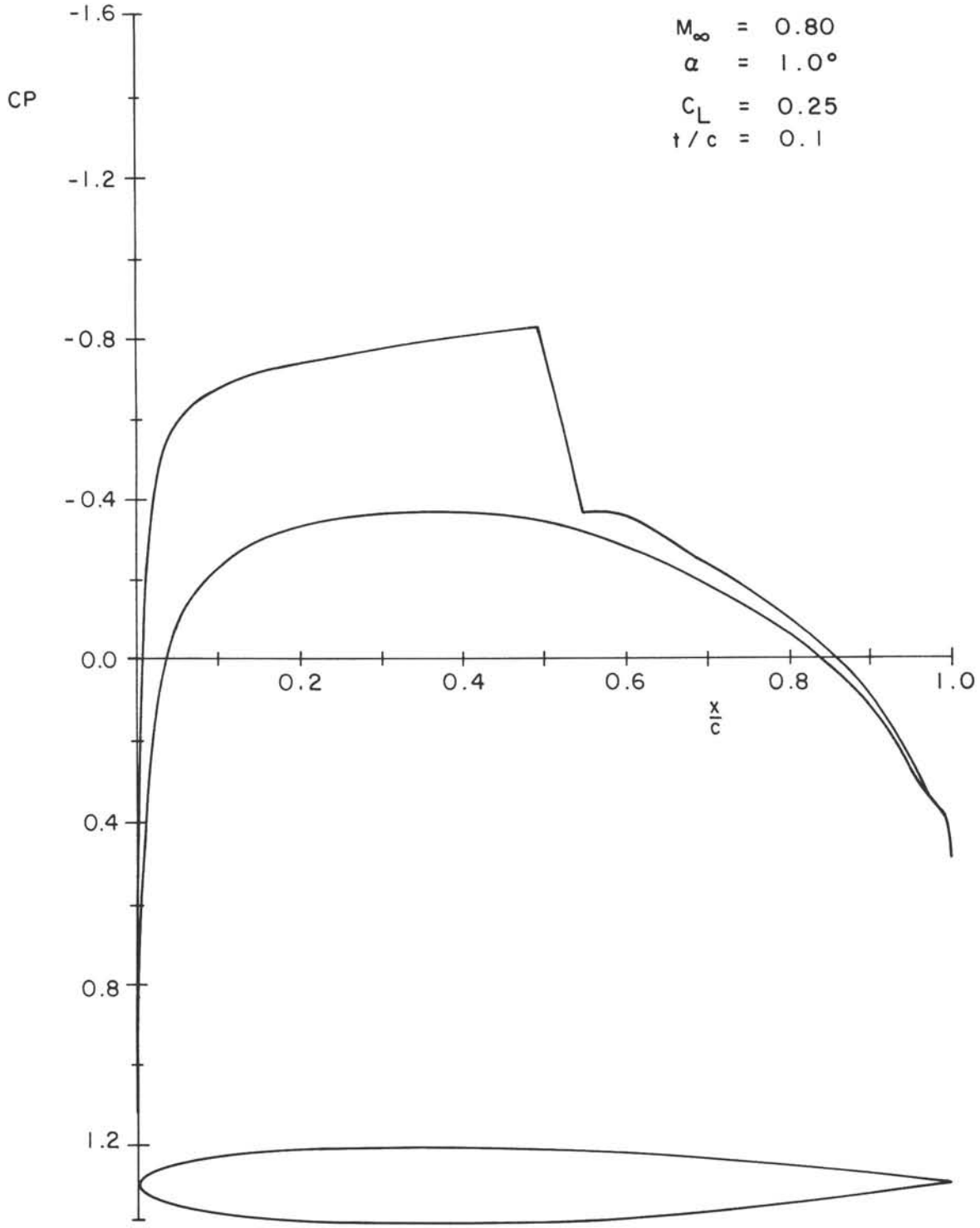

FIG. 1: TWO-DIMENSIONAL PRESSURE DISTRIBUTIONS OF THE AIRFOIL USED IN THE WING DESIGN

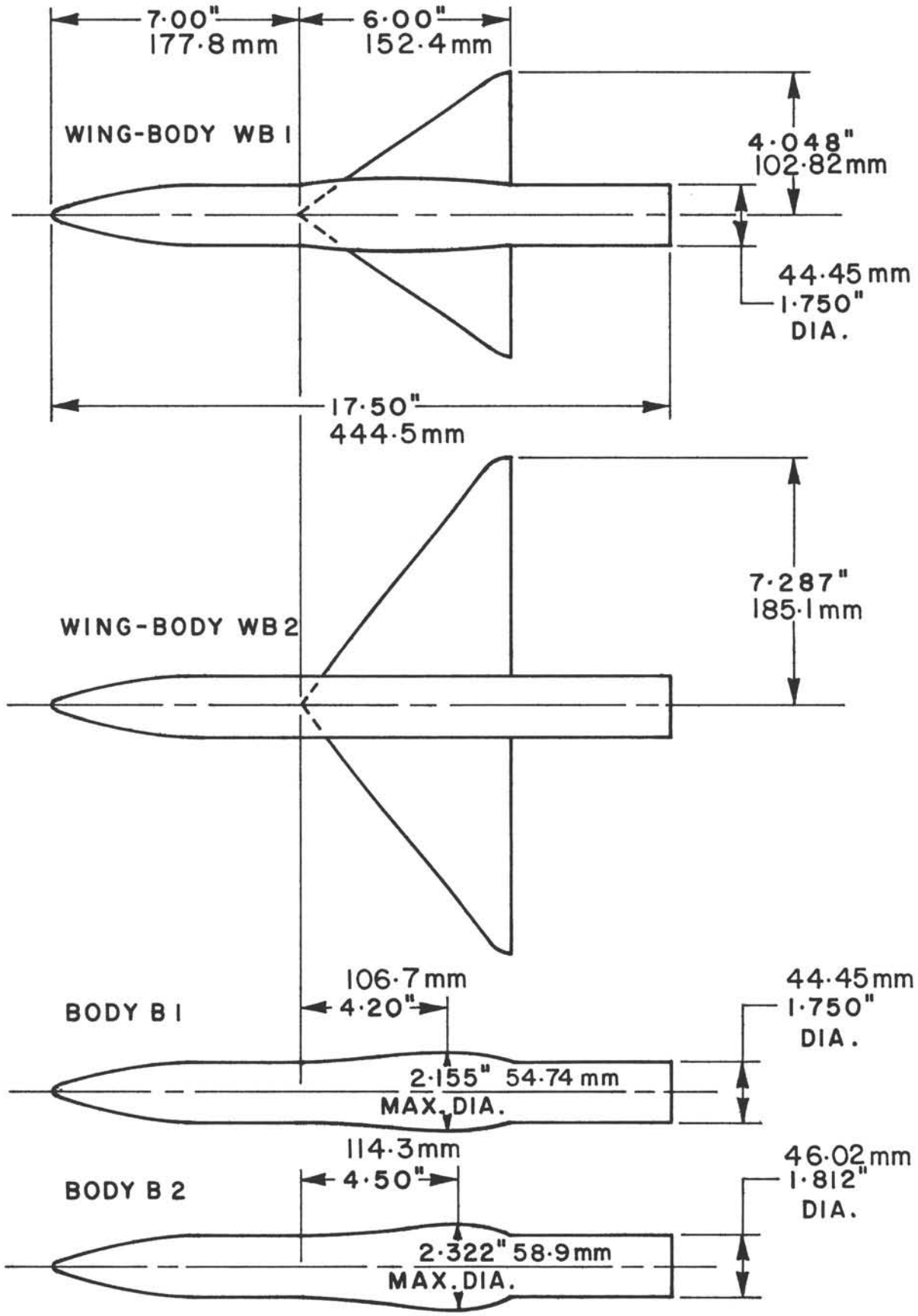

FIG. 2: THE WING-BODY COMBINATIONS AND THE EQUIVALENT BODIES

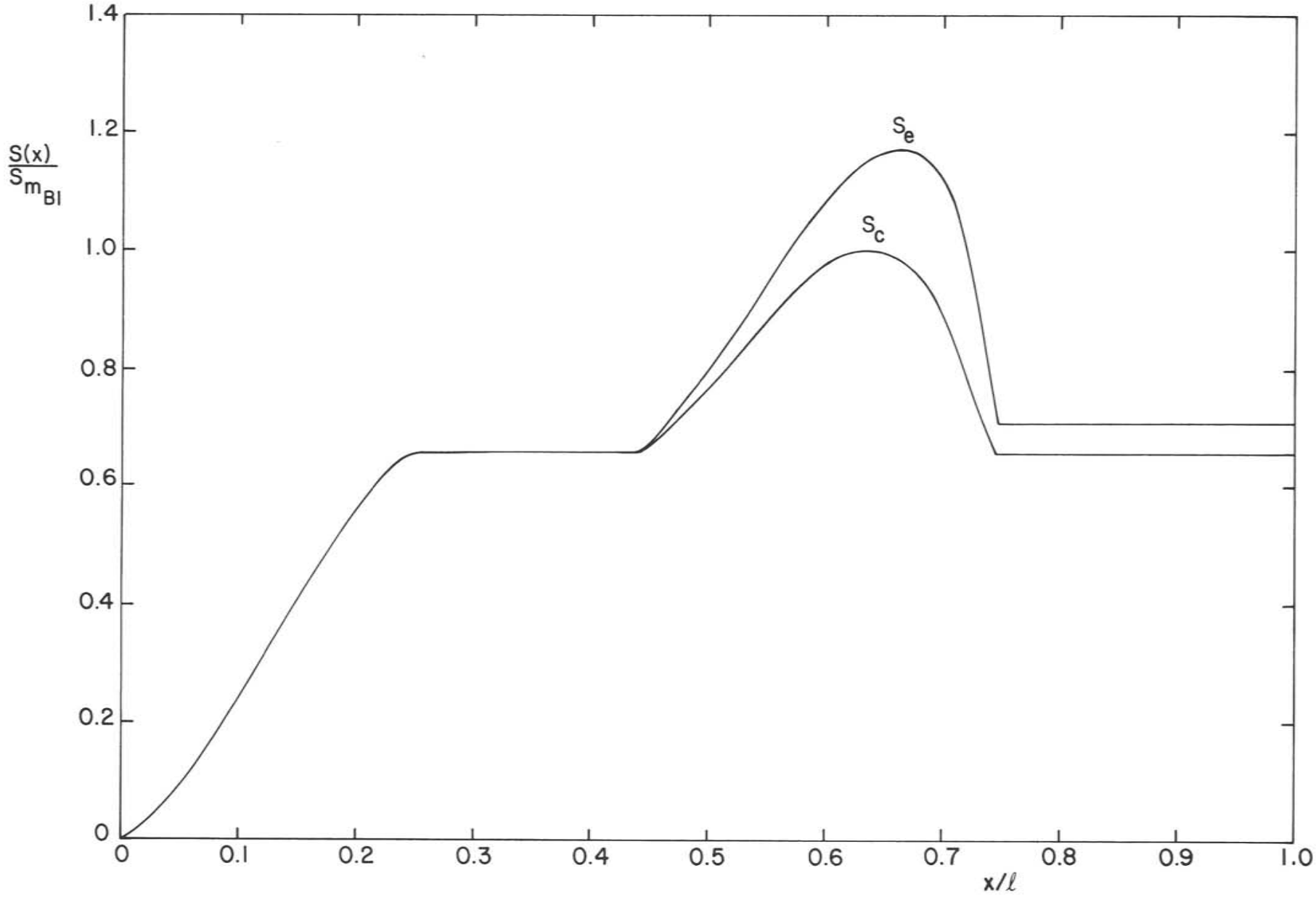

FIG. 3: CROSS-SECTIONAL AREA DISTRIBUTIONS OF THE MODELS WITH AND WITHOUT LIFT

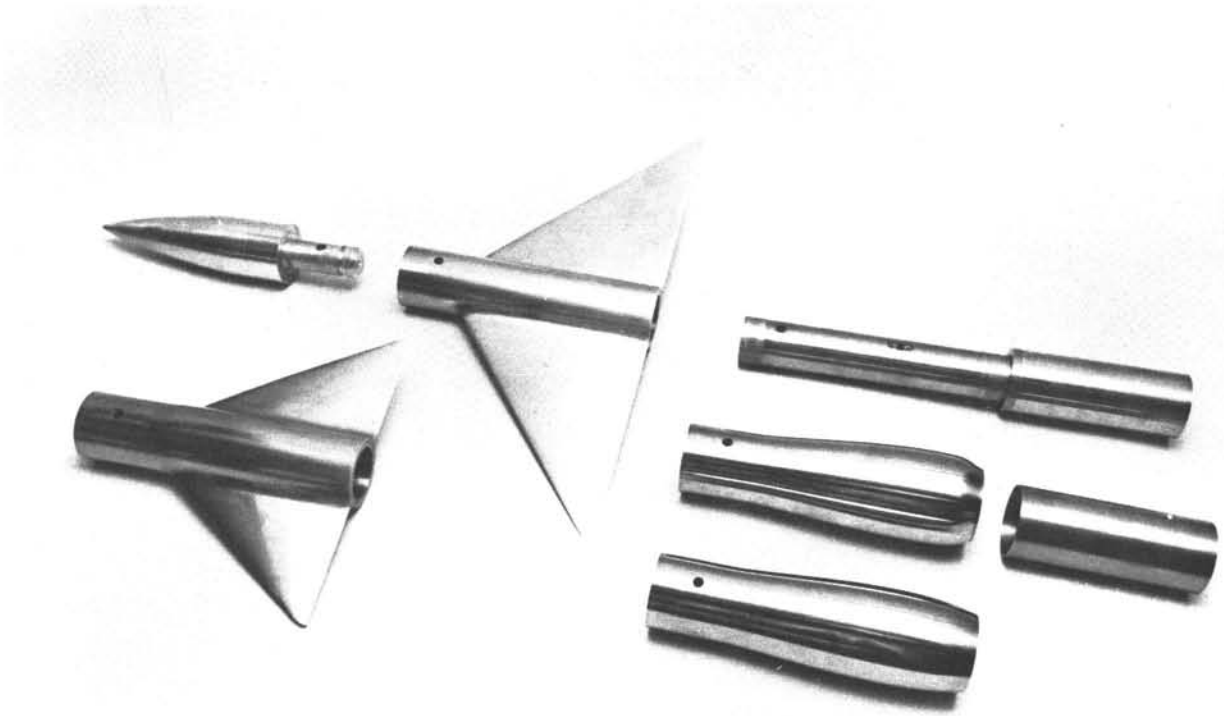

FIG. 4: MODEL PARTS BEFORE ASSEMBLY

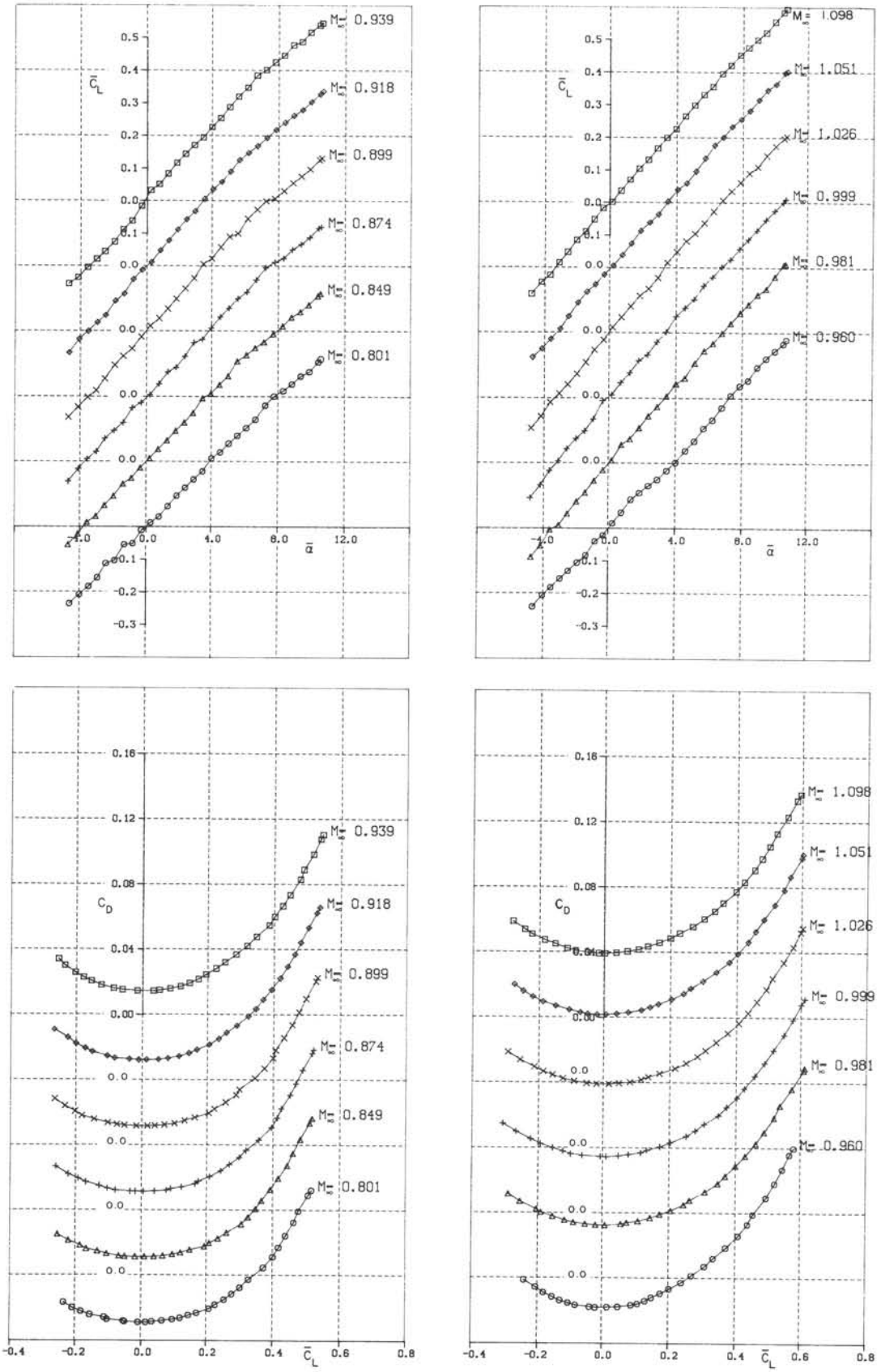

FIG. 5: VARIATION OF $\bar{C}_L$ WITH $\bar{\alpha}$ AND C_D WITH $\bar{C}_L$ FOR THE WING-BODY MODEL WB1 AT DIFFERENT MACH NUMBERS

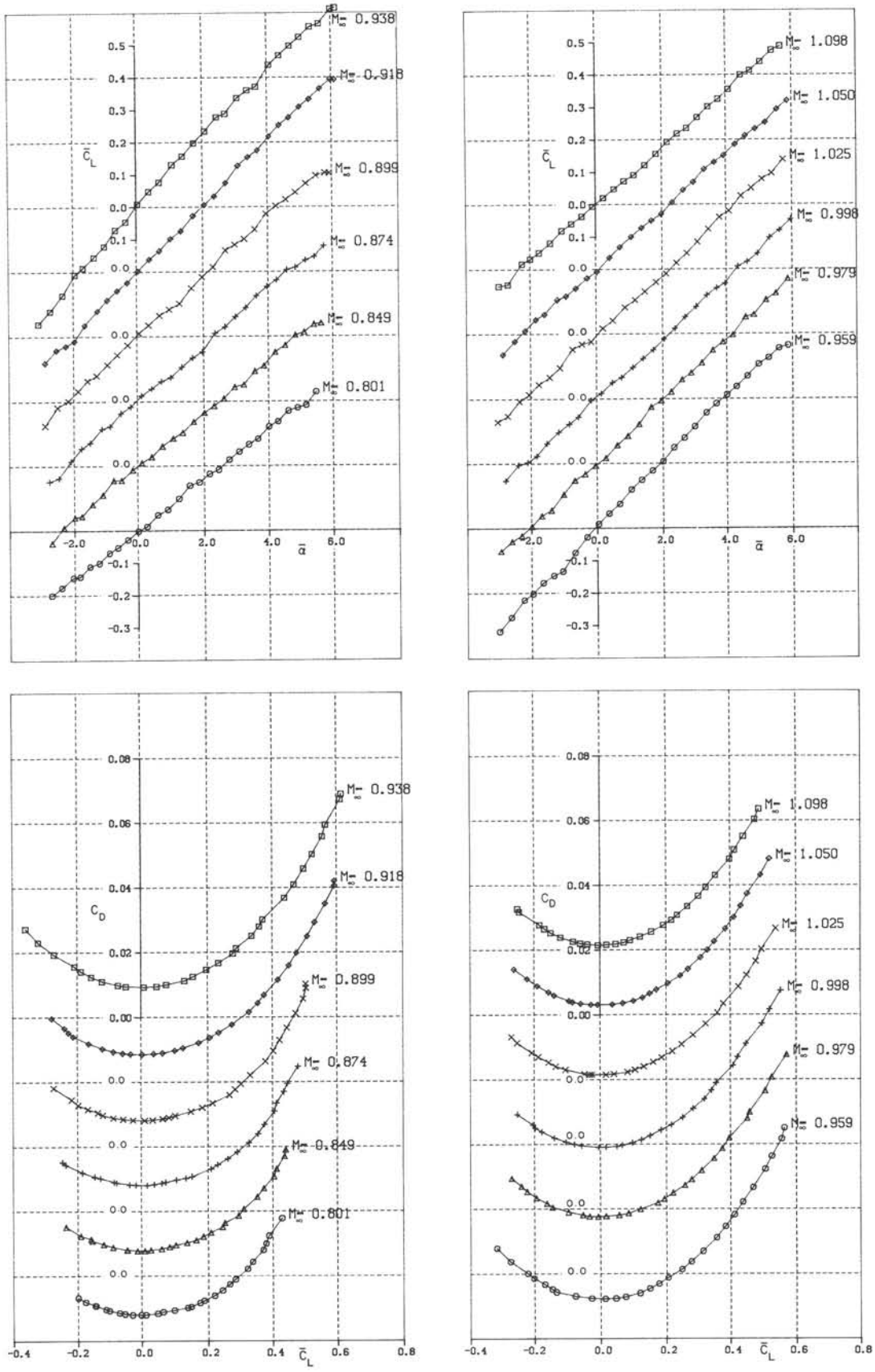

FIG. 6: VARIATION OF $\bar{C}_L$ WITH $\bar{\alpha}$ AND C_D WITH $\bar{C}_L$ FOR THE WING-BODY MODEL WB2 AT DIFFERENT MACH NUMBERS

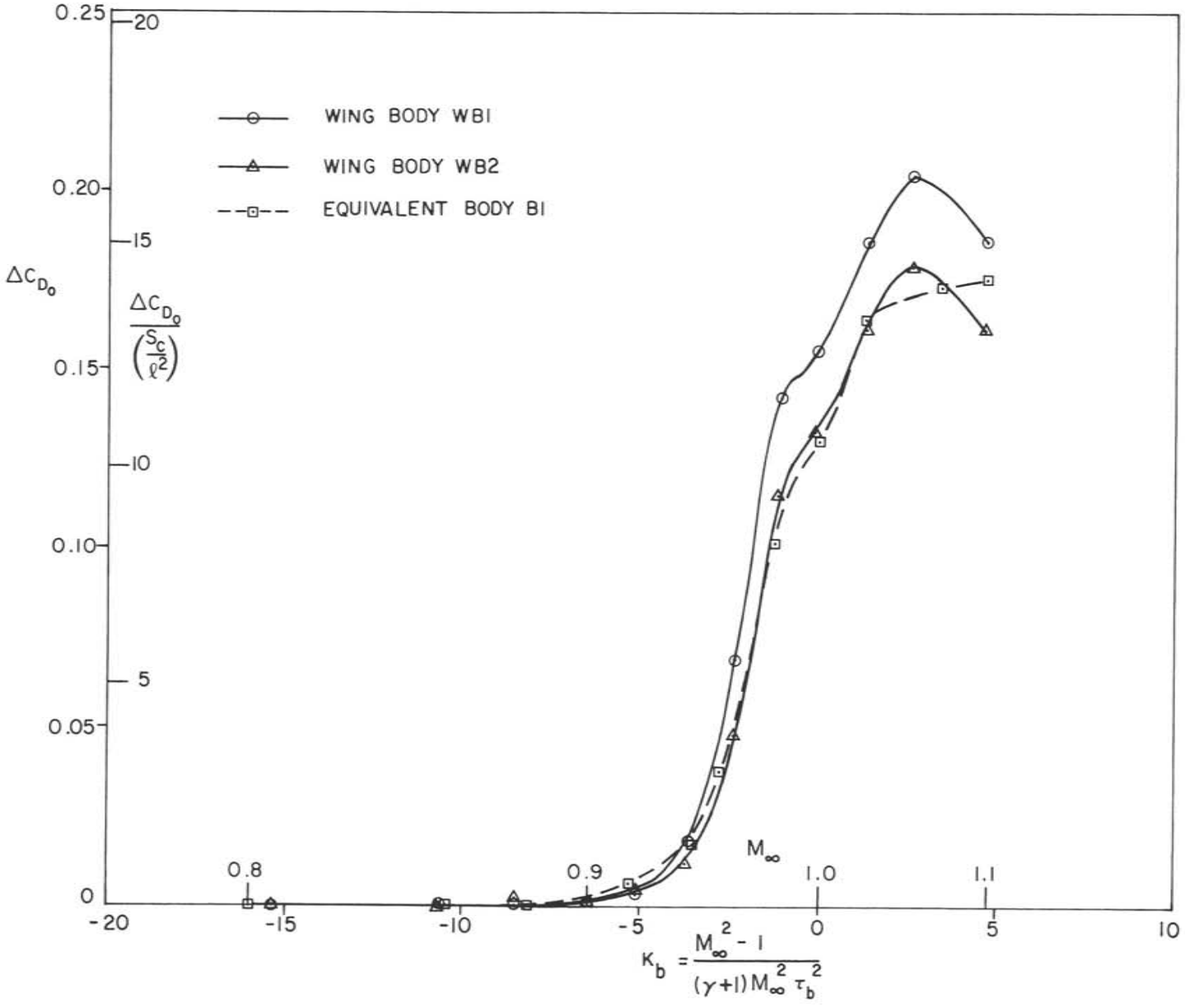

FIG. 7: ZERO LIFT DRAG-RISE FOR THE WING-BODIES WB1, WB2 AND THE BODY OF REVOLUTION B1

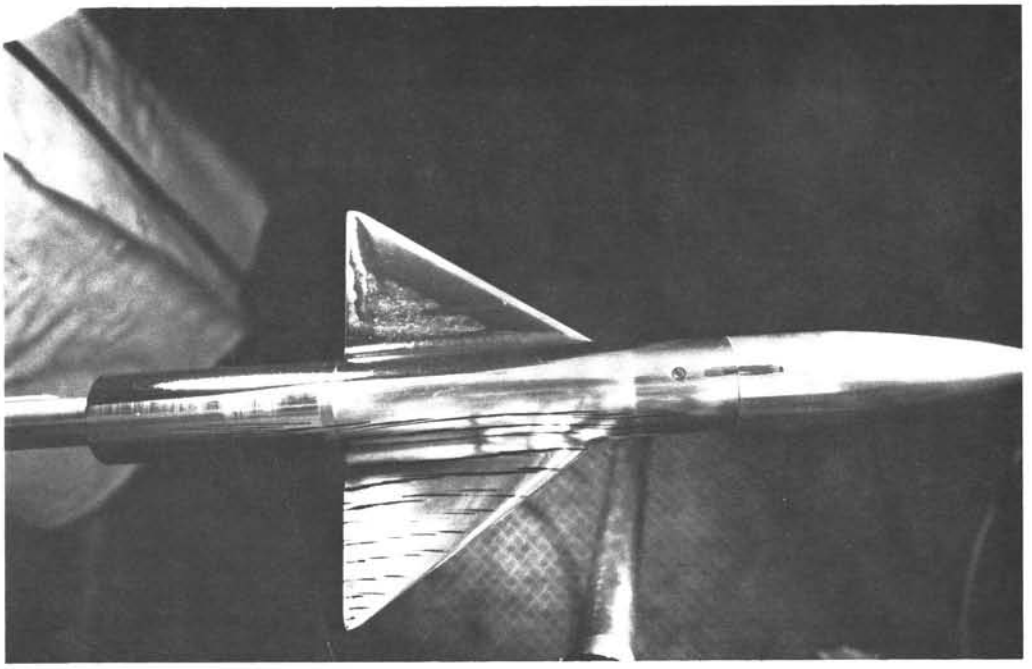

MODEL WB1

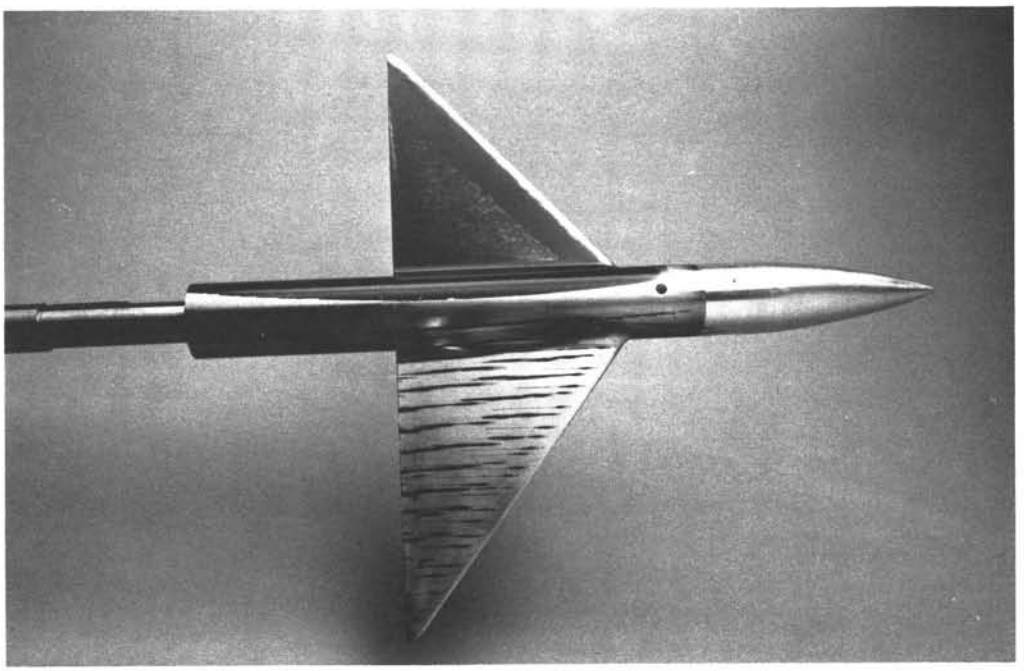

MODEL WB2

FIG. 8: SURFACE FLOW VISUALIZATION FOR THE WING-BODIES WB1 AND WB2 AT ZERO ANGLE OF ATTACK, $M_\infty = 0.96$

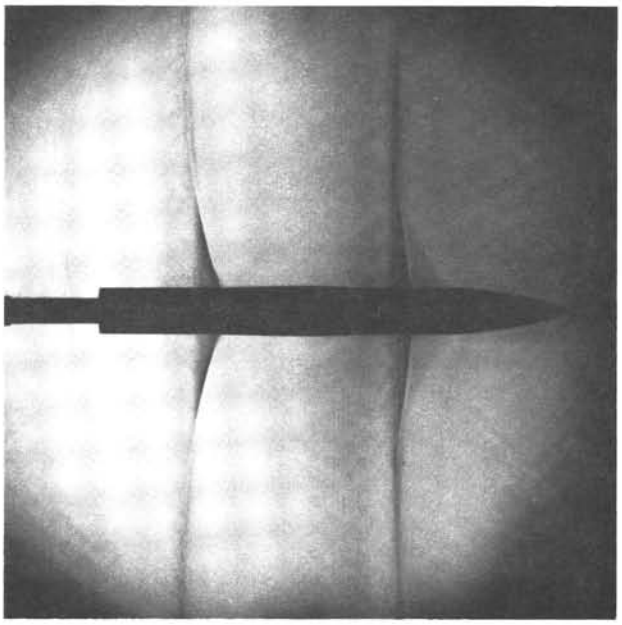

WB1, $\bar{\alpha} = -0.12°$

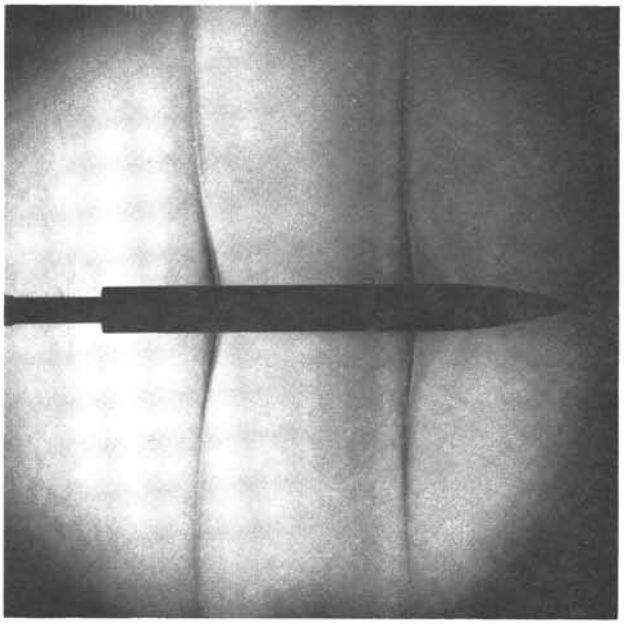

WB2, $\bar{\alpha} = 0.22°$

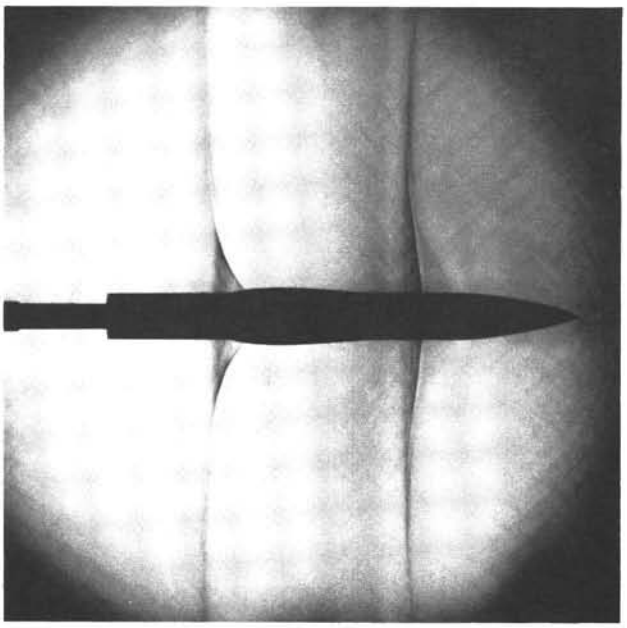

B2, $\bar{\alpha} = -0.05°$

FIG. 9: SCHLIEREN FLOW VISUALIZATION FOR WING-BODIES WB1, WB2 AND BODY OF REVOLUTION B1 AT ZERO ANGLE OF ATTACK (NOMINAL), $M_\infty = 0.98$

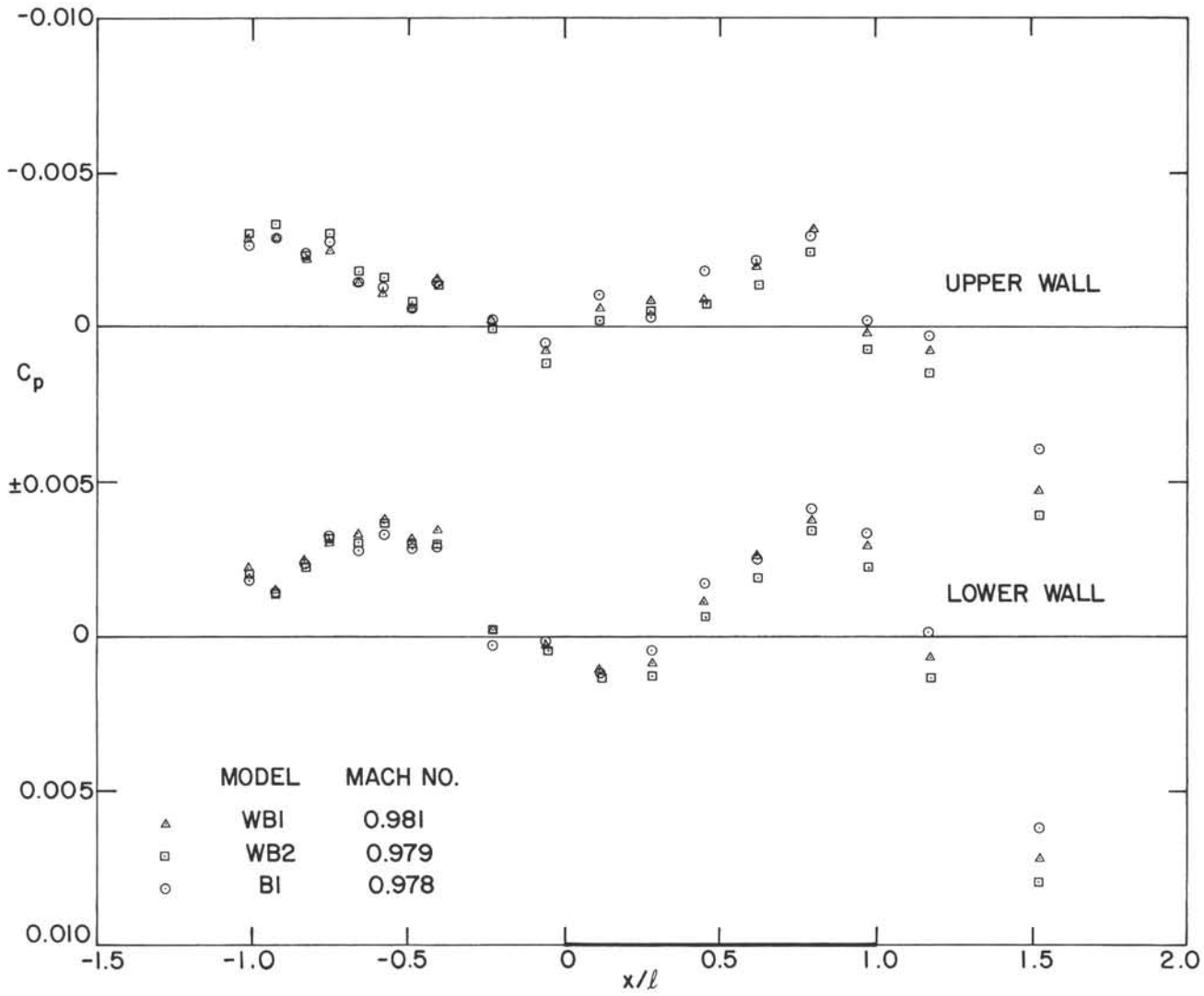

FIG. 10: STATIC PRESSURE DISTRIBUTIONS NEAR THE UPPER AND THE LOWER WALLS OF THE TEST SECTION FOR THE WING-BODIES WB1, WB2 AND THE BODY OF REVOLUTION B1 AT ZERO ANGLE OF ATTACK, M_∞ = 0.98

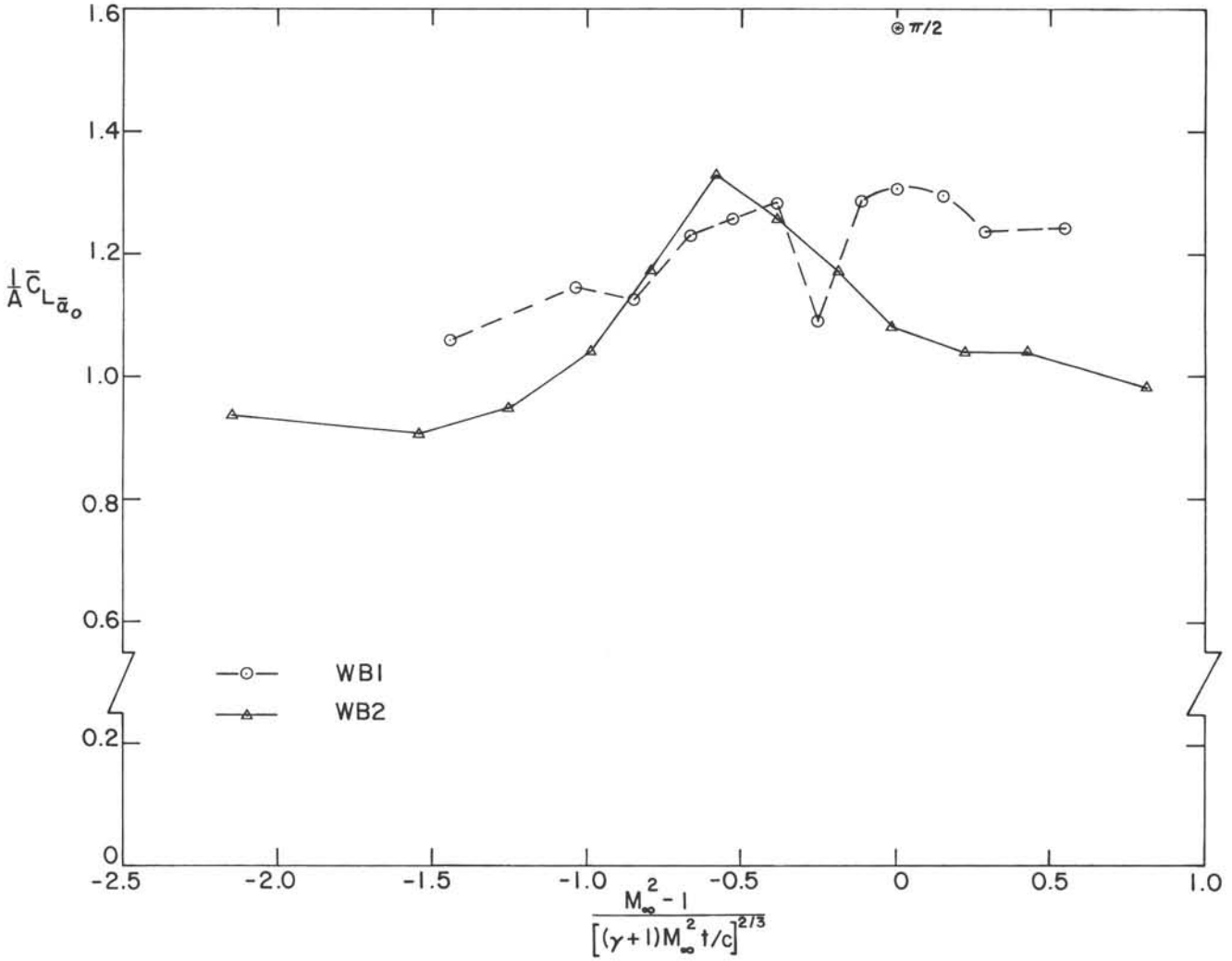

FIG. 11: VARIATION OF LIFT CURVE SLOPE AT ZERO LIFT WITH TRANSONIC SIMILARITY PARAMETER BASED ON THE WING THICKNESS TO CHORD RATIO FOR THE WING-BODIES WB1 AND WB2

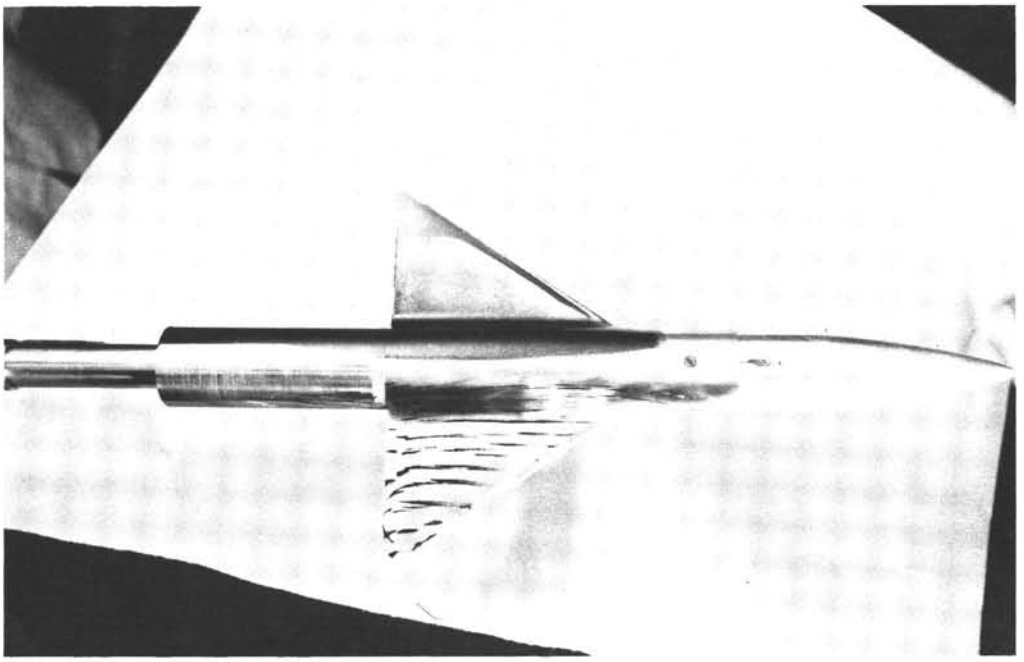

MODEL WB1, α = 5.06°

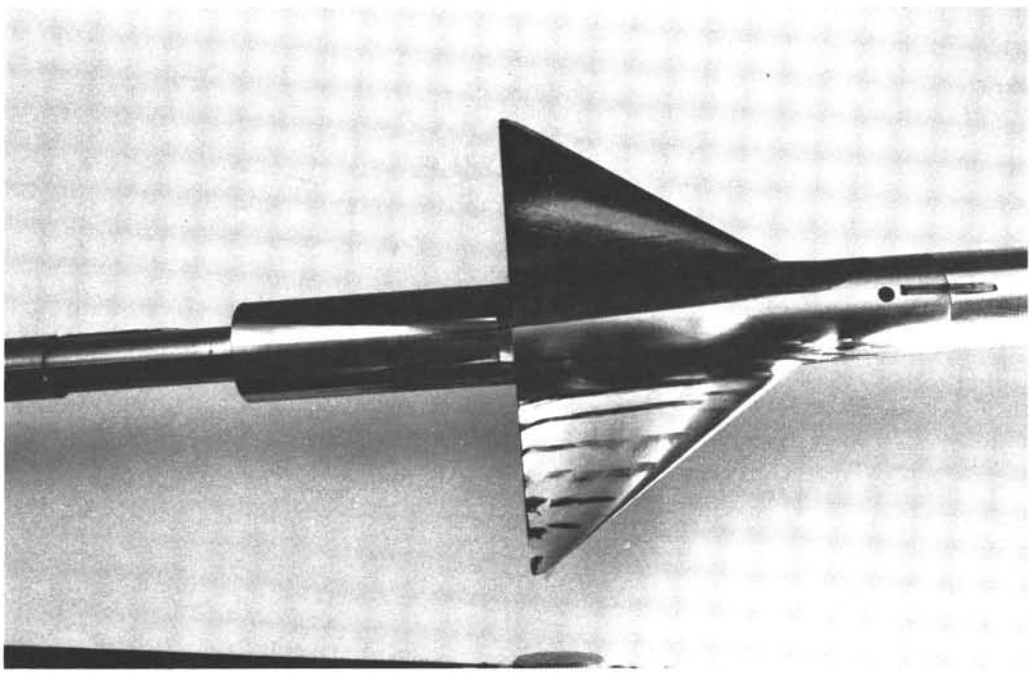

MODEL WB1, α = 10.09°

FIG. 12(a): SURFACE FLOW VISUALIZATION FOR THE WING-BODIES WB1 AND WB2 AT ANGLE OF ATTACK, M_∞ = 0.96

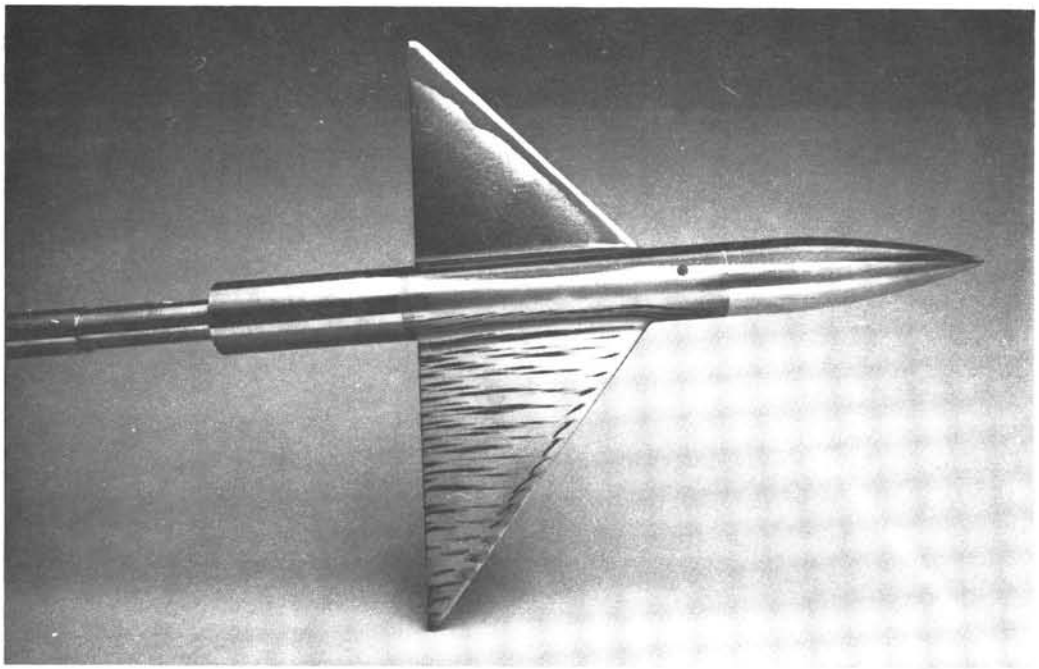

MODEL WB2, α = 2.56°

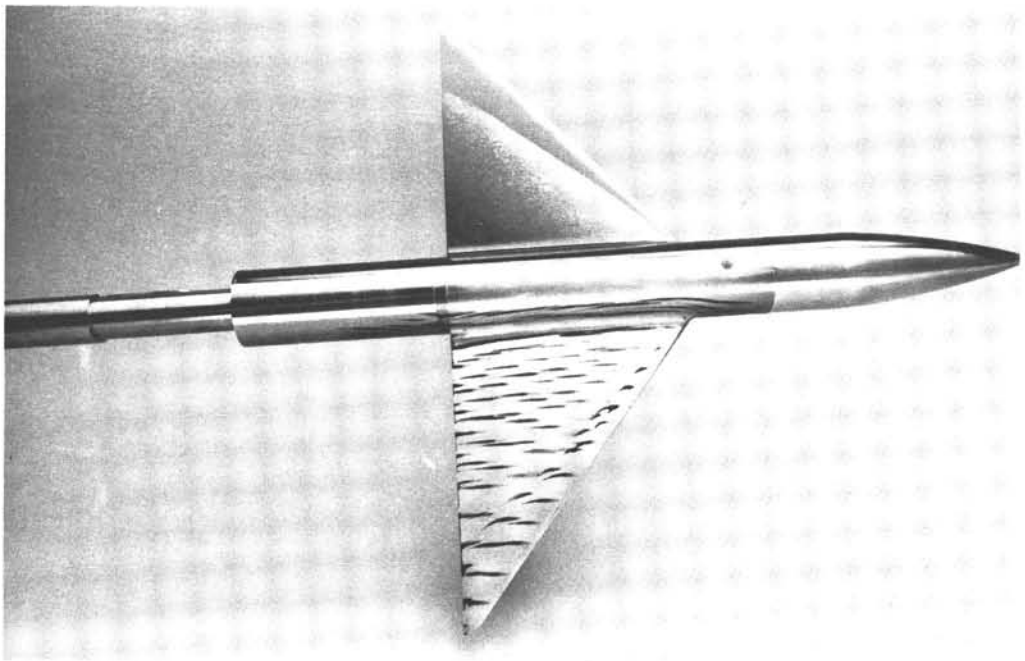

MODEL WB2, α = 5.05°

FIG. 12(b): SURFACE FLOW VISUALIZATION FOR THE WING-BODIES WB1 AND WB2 AT ANGLE OF ATTACK, M_∞ = 0.96

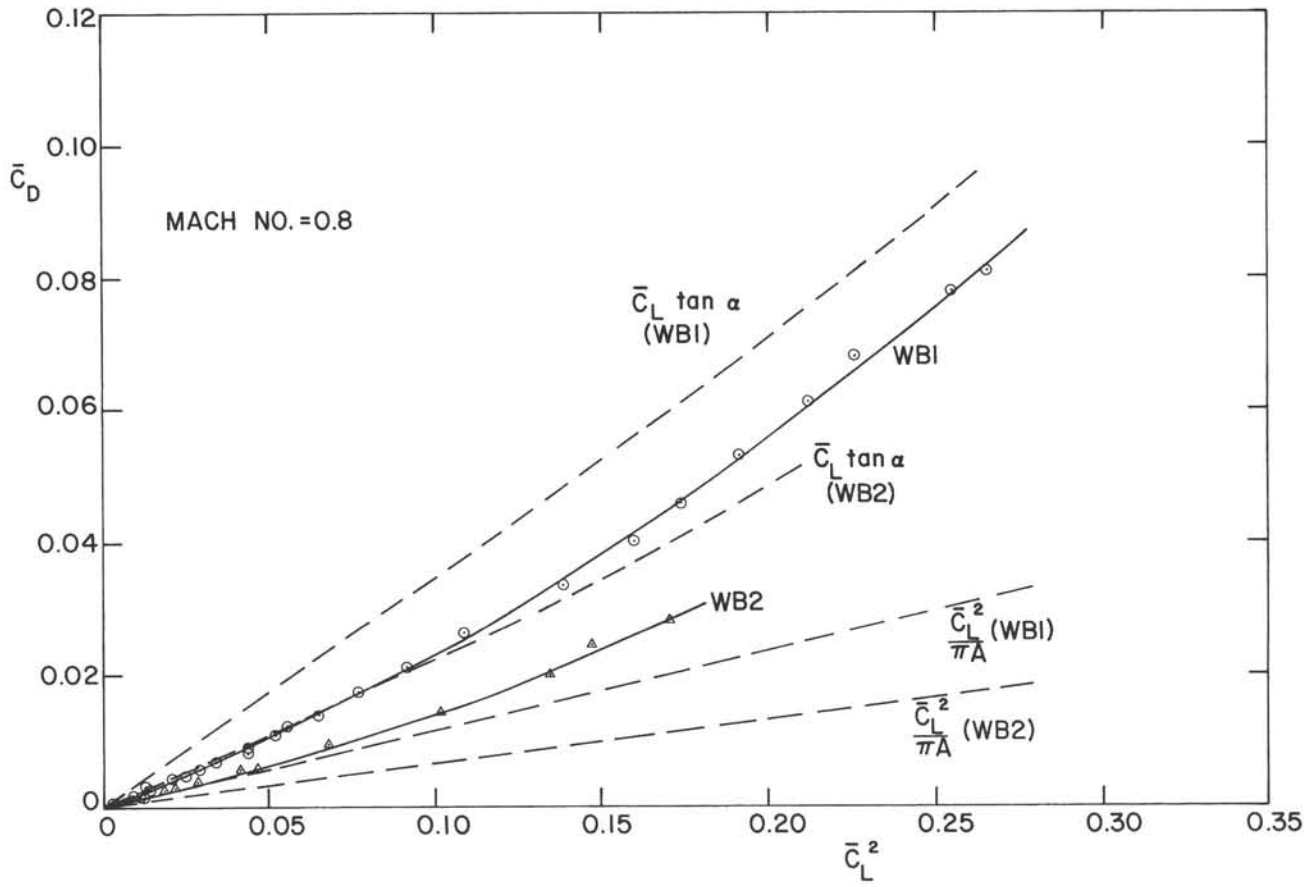

FIG. 13: VARIATION OF $\bar{C}_D$ WITH $\bar{C}_L^2$ FOR THE WING-BODIES WB1 AND WB2 AT MACH NUMBER 0.8

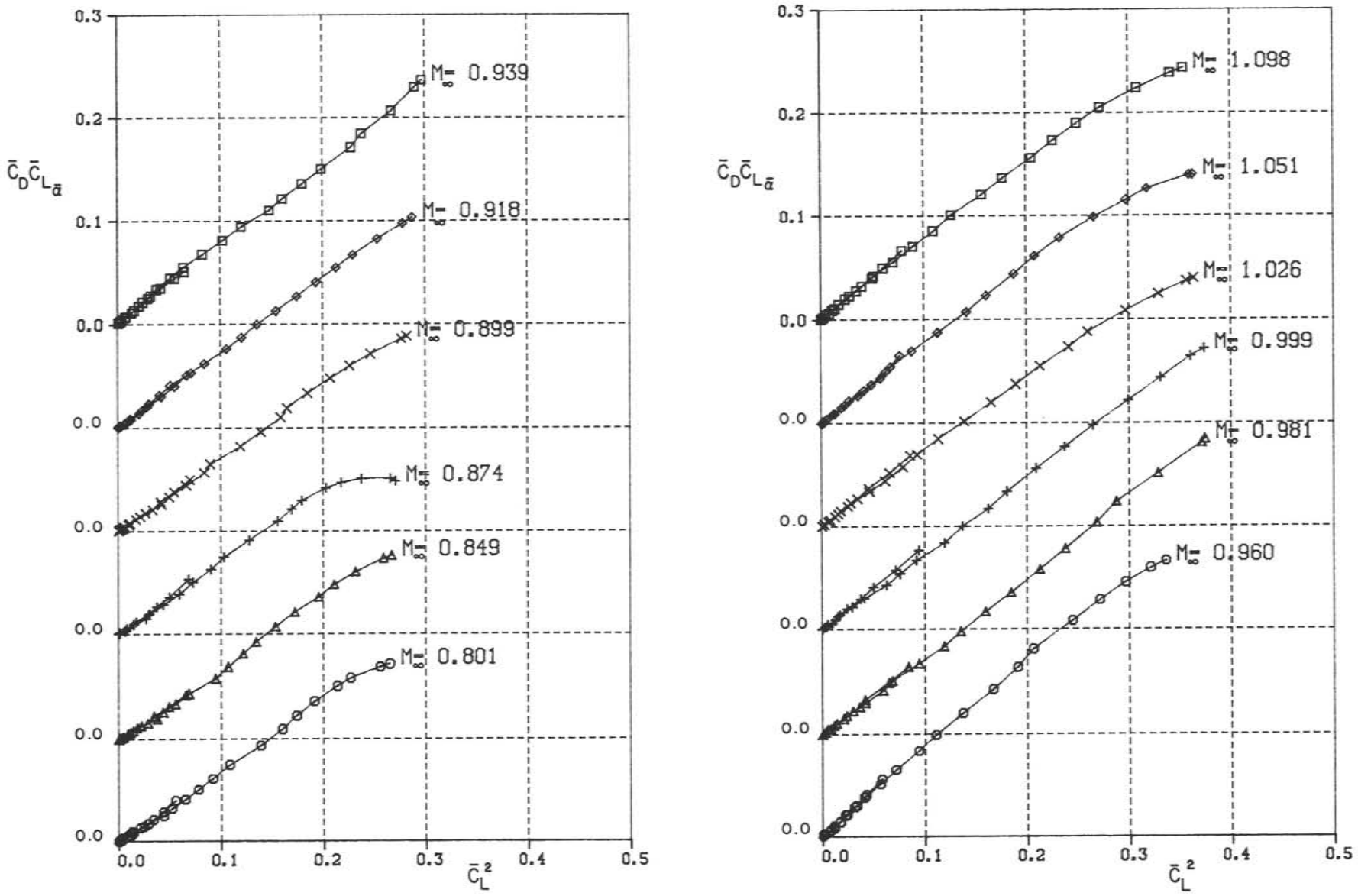

FIG. 14: VARIATION OF $\bar{C}_D\bar{C}_{L_{\bar{\alpha}}}$ WITH $\bar{C}_L{}^2$ FOR THE WING-BODY WB1 AT DIFFERENT MACH NUMBERS

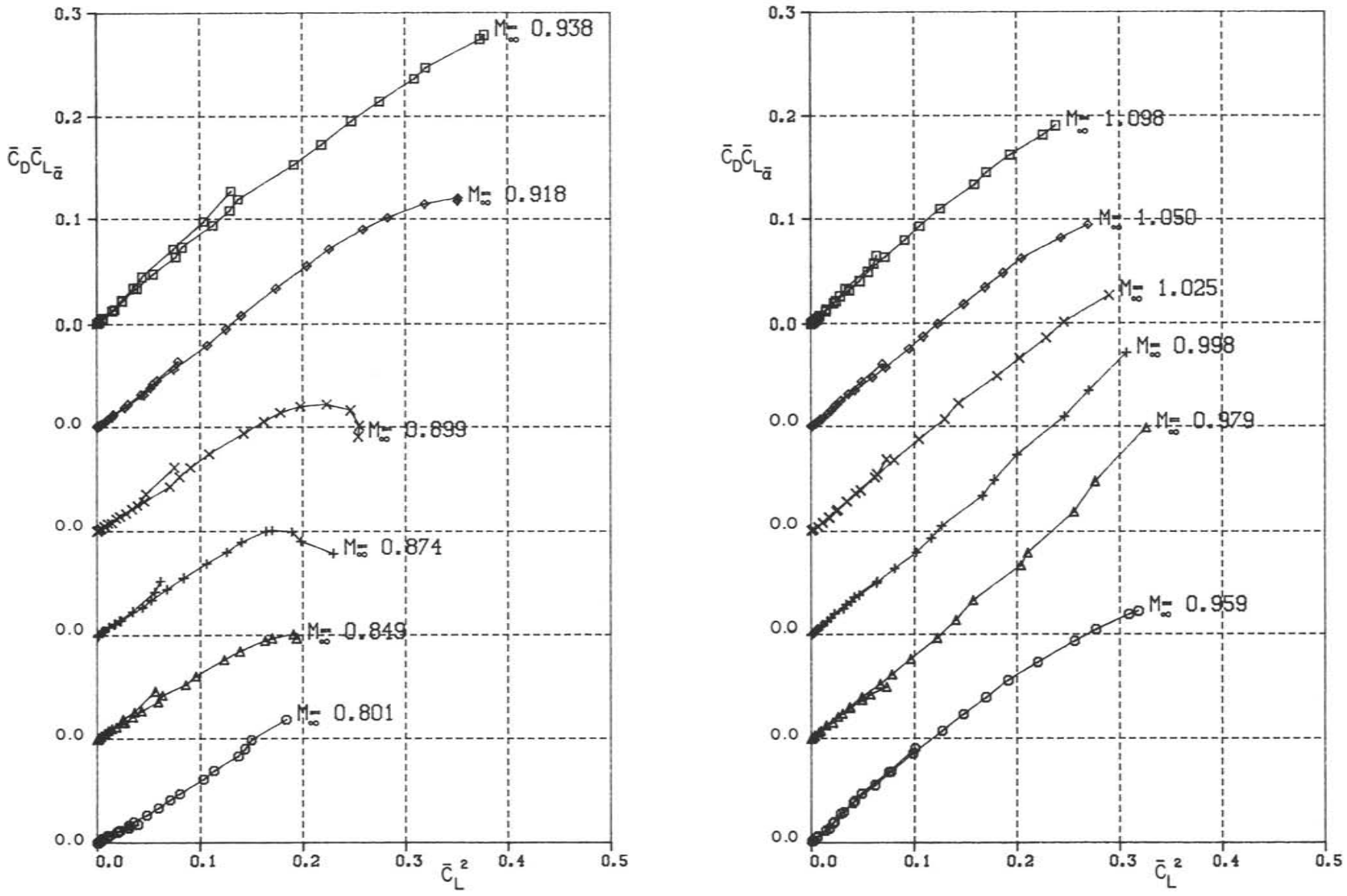

FIG. 15: VARIATION OF $\bar{C}_D\bar{C}_{L_{\bar{\alpha}}}$ WITH $\bar{C}_L^2$ FOR THE WING-BODY WB2 AT DIFFERENT MACH NUMBER

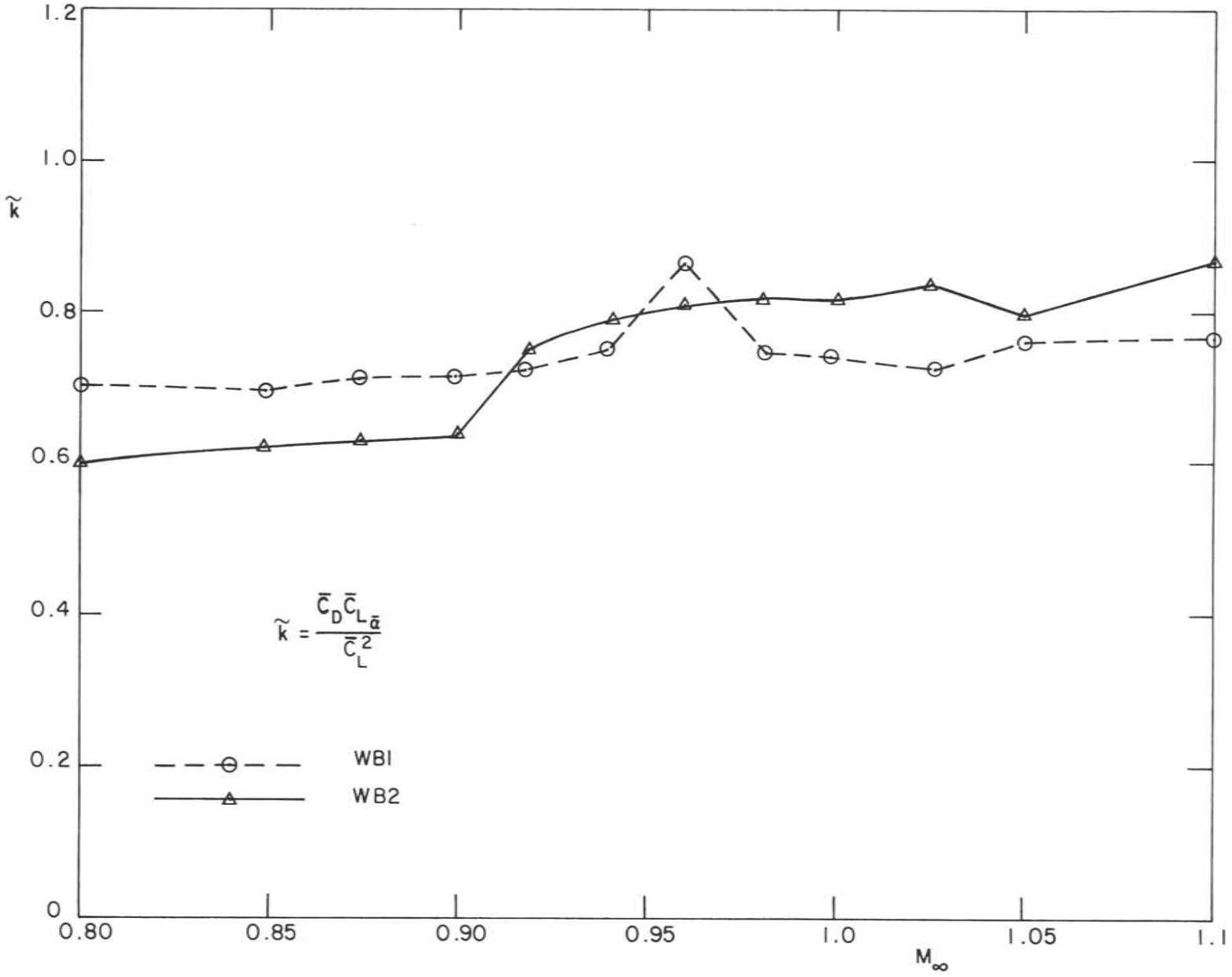

FIG. 16: VARIATION OF THE INDUCED DRAG FACTOR $\tilde{k}$ WITH MACH NUMBER FOR THE WING-BODIES WB1 AND WB2

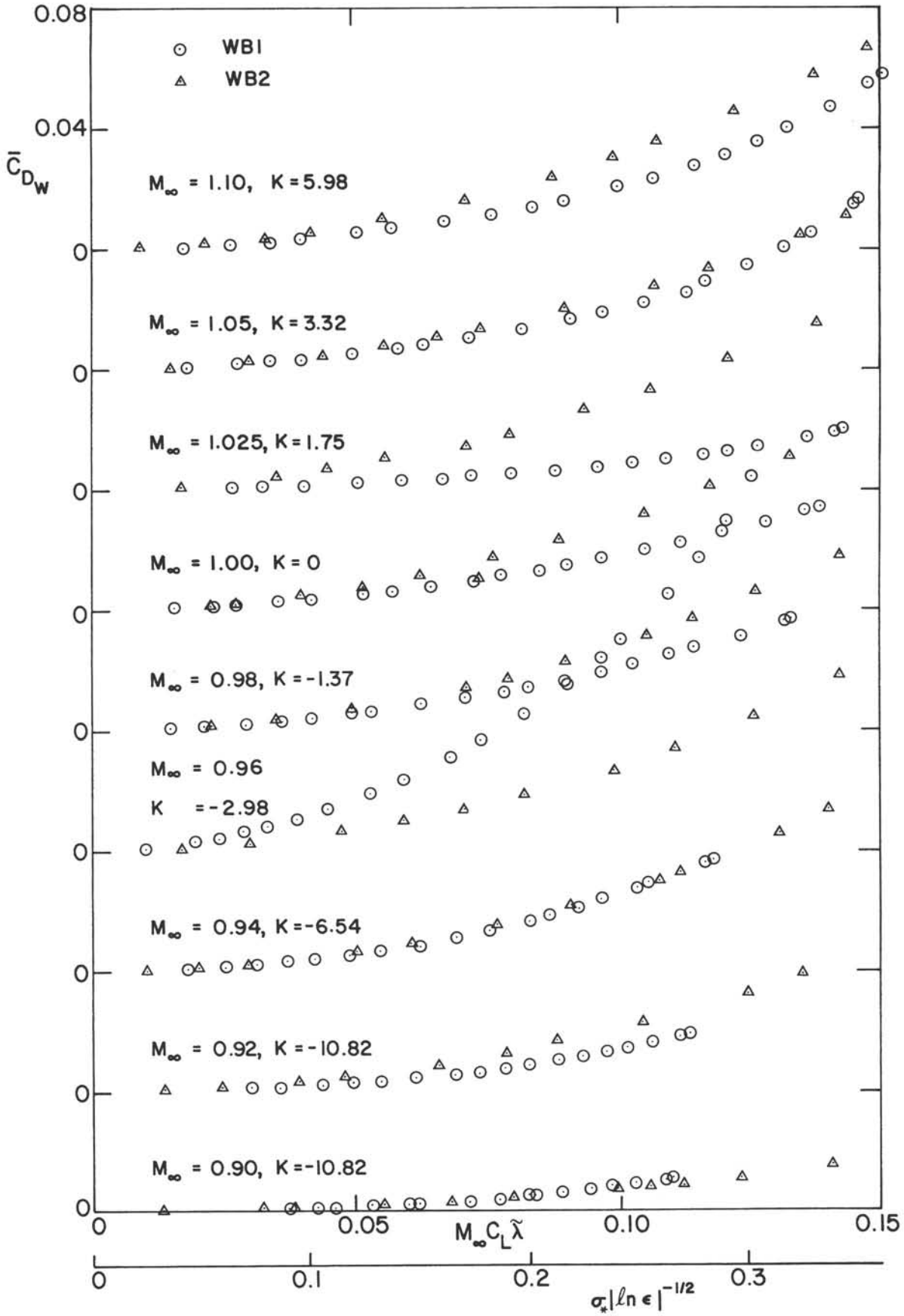

FIG. 17: VARIATION OF WAVE DRAG $\bar{C}_{D_w}$ WITH LIFT PARAMETERS FOR THE WING-BODIES WB1 AND WB2

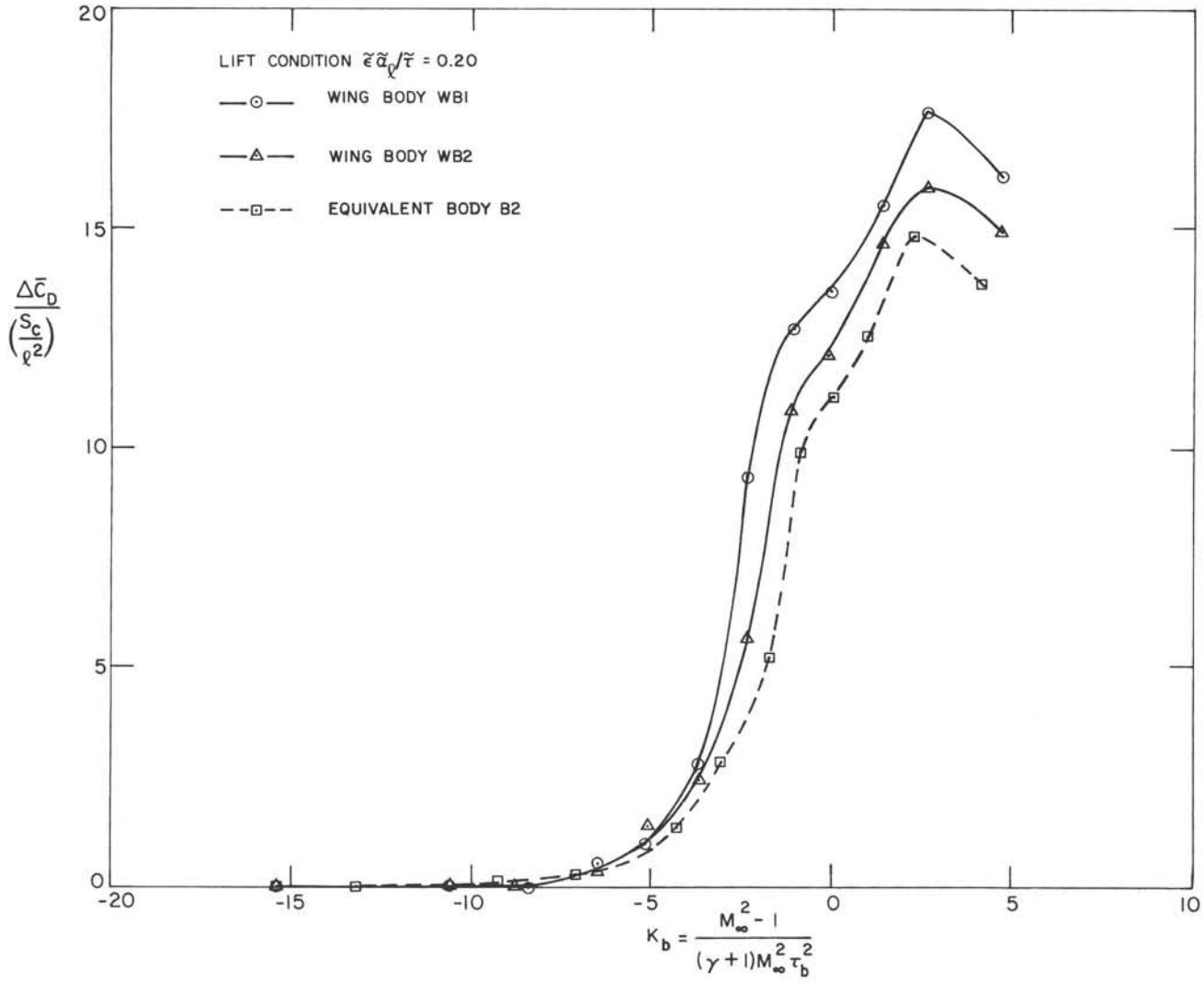

FIG. 18: DRAG-RISE FOR THE WING-BODIES WB1, WB2 AND THE BODY OF REVOLUTION B2 AT THE DESIGN LIFT CONDITION

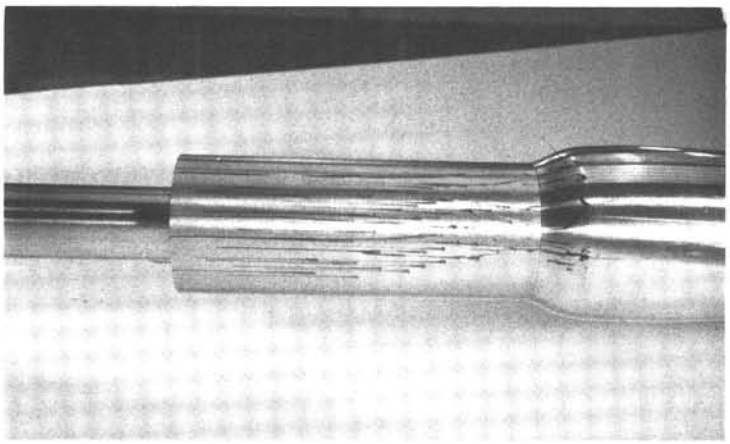

FIG. 19: SURFACE FLOW VISUALIZATION FOR THE BODY OF REVOLUTION B2 AT MACH NUMBER 0.96

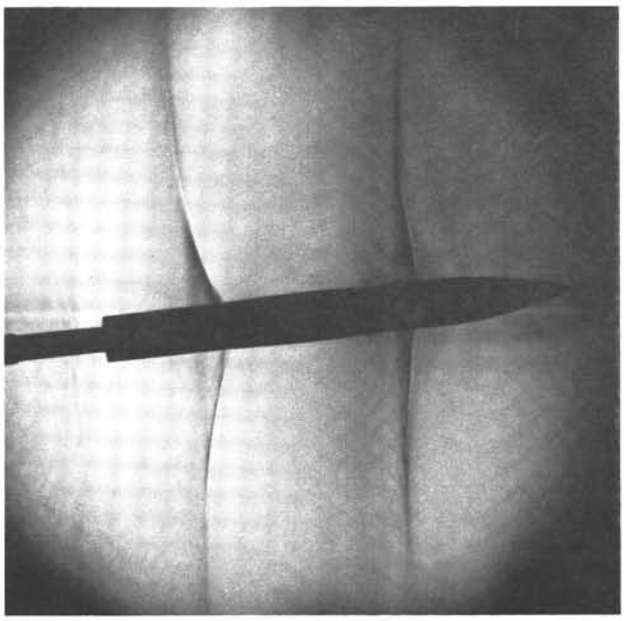

WBI, $\bar{\alpha}$ = 5.69°, $M_\infty \bar{C}_L \tilde{\lambda}$=0.0784

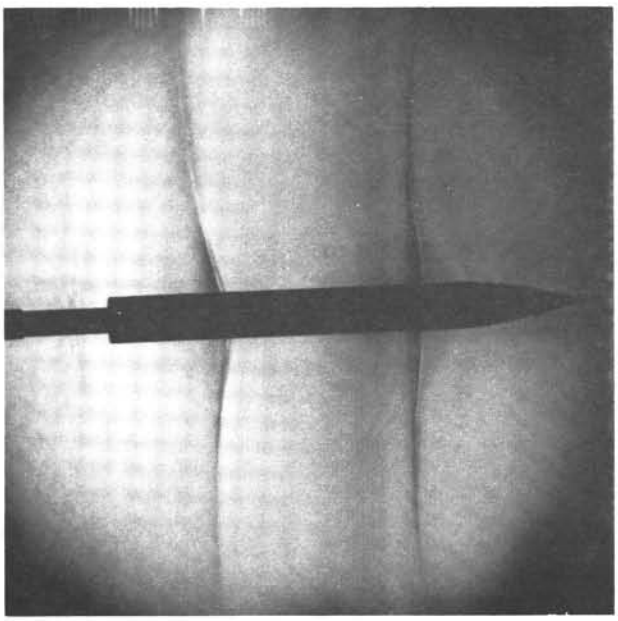

WB2, $\bar{\alpha}$ = 2.06°, $M_\infty \bar{C}_L \tilde{\lambda}$ = 0.0827

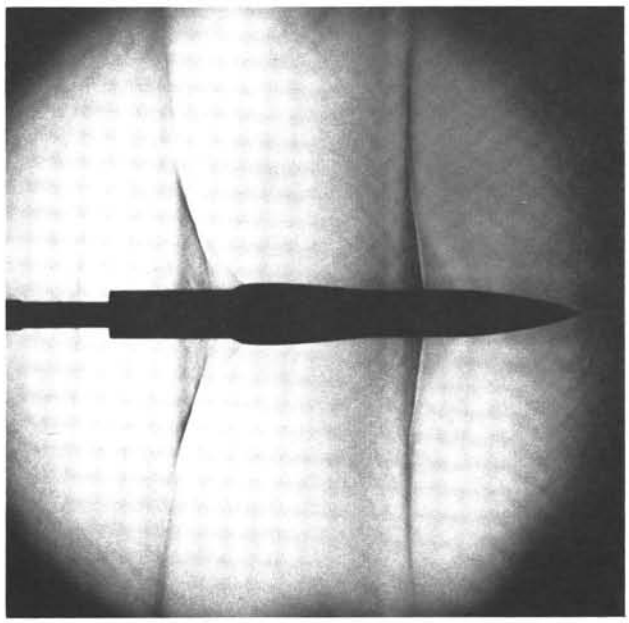

B2, α = 0.06°

FIG. 20: SCHLIEREN FLOW VISUALIZATION FOR THE WING-BODIES WB1, WB2 AT INCIDENCE AND THE BODY OF REVOLUTION B2, M_∞ = 0.98

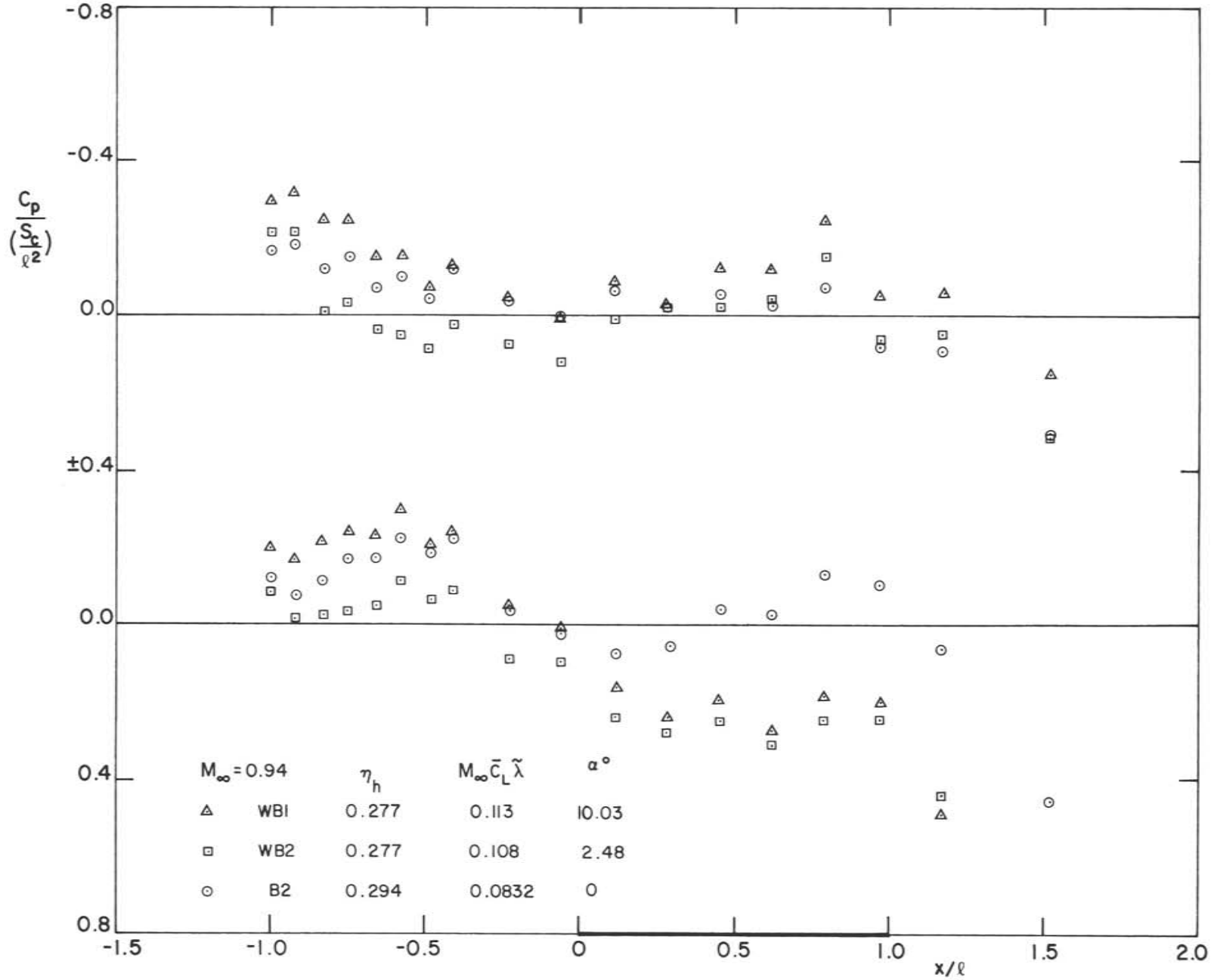

FIG. 21: STATIC PRESSURE DISTRIBUTIONS NEAR THE UPPER AND THE LOWER WALLS OF THE TEST SECTION FOR THE WING-BODIES WB1 AND WB2 AT THE SAME LIFT PARAMETER, M_∞ = 0.94

APPENDIX A

SIMILARITY PARAMETERS OF THREE-DIMENSIONAL TRANSONIC FLOWS

Similarity parameters of a physical problem can be derived from the governing differential equations and the boundary conditions. For three-dimensional transonic flow with small disturbances the parameters come about naturally in the derivation of the small disturbance equations. With the flow taken to be uniform upstream in the x-direction, the velocity components and the density of the flow can be written for a small disturbance

$$\begin{aligned} u^* &= U_\infty (1 + \Delta u) \\ v^* &= U_\infty \Delta v \\ w^* &= U_\infty \Delta w \\ \rho^* &= \rho_\infty (1 + \Delta \rho) \end{aligned} \tag{A1}$$

where Δ is a perturbation parameter to be determined from the small disturbance condition, i.e. the boundary condition on the body. The co-ordinates are scaled as follows

$$\begin{aligned} x^* &= \ell\, x \\ y^* &= b\, y \\ z^* &= c\, z \end{aligned} \tag{A2}$$

where ℓ, b and c are the typical lengths of the body in their respective co-ordinate directions. If the body surface is given by the expression

$$z^* = \delta\, f^* (x^*, y^*) \tag{A3}$$

where δ is small, so that the requirement for small disturbance is satisfied, we can show that

$$\Delta \sim 0(\delta) \tag{A4}$$

The governing equations chosen for the derivation of the small disturbance equation are the conservation equations of mass and energy. These equations satisfy automatically the discontinuity conditions of the shock wave which may occur in the flow field.

$$\begin{aligned} &(\rho^* u^*)_{x^*} + (\rho^* v^*)_{y^*} + (\rho^* w^*)_{z^*} = 0 \\ &\frac{1}{2}(u^{*2} + v^{*2} + w^{*2}) + \frac{a^{*2}}{\gamma - 1} = \frac{1}{2} U_\infty^{*2} + \frac{a_\infty^{*2}}{\gamma - 1} \end{aligned} \tag{A5}$$

With the perturbation velocities Equation (A1) and eliminating the density with the energy equation

$$\frac{\rho^*}{\rho_\infty^*} = 1 + \Delta\rho = 1 - M_\infty^2 \left[\Delta u + \frac{1}{2}(\Delta v)^2 + \frac{1}{2}(\Delta w)^2\right] + \left[(2 - \gamma) M_\infty^2 - 1\right] \frac{M_\infty^2}{2} (\Delta u)^2 + \ldots \tag{A6}$$

the perturbation equation for the velocity is derived up to the second order

$$\frac{\Delta}{\ell}(1-M_\infty^2)u_x + \frac{\Delta}{b}v_y + \frac{\Delta}{c}w_z - \frac{M_\infty^2}{2}\frac{\Delta^2}{\ell}(v^2+w^2)_x - \frac{\Delta^2}{\ell}(\gamma+1)\frac{M_\infty^2}{2}(u^2)_x$$

$$- M_\infty^2\Delta^2\left(\frac{1}{b}u_y v + \frac{1}{c}u_z w\right) - M_\infty^2\Delta^2\left(\frac{1}{b}uv_y + \frac{1}{c}uw_z\right) = 0 \qquad \text{A7}$$

Assuming that the flow is irrotational and introducing a velocity potential

$$\Phi^* = U_\infty x^* + \phi^* = U_\infty \ell\,(x + \Delta\phi) \qquad \text{(A8)}$$

with

$$u = \frac{\partial\phi}{\partial x}, \qquad v = \frac{\ell}{b}\frac{\partial\phi}{\partial y}, \qquad w = \frac{\ell}{c}\frac{\partial\phi}{\partial z}$$

The velocity equation can be written in terms of ϕ as

$$\left[(1-M_\infty) - \Delta(\gamma+1)M_\infty\phi_x\right]\phi_{xx} + \frac{\ell^2}{b^2}\phi_{yy} + \frac{\ell^2}{c^2}\phi_{zz} = \Delta M_\infty^2\left[\frac{\ell^2}{b^2}\phi_y + \frac{\ell^2}{c^2}\phi_z^2\right]_x$$

$$+ \Delta M_\infty^2\left[\frac{\ell^2}{b^2}\phi_{yy} + \frac{\ell^2}{c^2}\phi_{zz}\right]\phi_x \qquad \text{(A9)}$$

For a configuration with small or moderate aspect ratio, the length scale c is taken as b, and Equation (A9) can be rearranged into the following form

$$\left[\frac{1-M_\infty^2}{(\gamma+1)M_\infty^2\Delta} - \phi_x\right]\phi_{xx} - \frac{1}{(\gamma+1)M_\infty^2\Delta}\frac{\ell^2}{b^2}(\phi_{yy}+\phi_{zz}) = \frac{1}{\gamma+1}\frac{\ell^2}{b^2}(\phi_y^2+\phi_z^2)_x$$

$$+ \frac{1}{\gamma+1}\frac{\ell^2}{b^2}(\phi_{yy}+\phi_{zz})\phi_x \qquad \text{(A10)}$$

The perturbation parameter now has the form

$$\Delta = \delta\left(\frac{b}{\ell}\right)^2 = \tau\lambda \qquad \text{(A11)}$$

where $\tau = \frac{\delta b}{\ell}$ and $\lambda = \frac{b}{\ell}$ are the thickness and the swept back parameters respectively. The boundary condition is therefore

$$\frac{\partial\phi}{\partial z} = \frac{\partial f(x,y)}{\partial x} - \frac{\alpha}{\tau} \quad \text{or} \quad y = 0 \qquad \text{(A12)}$$

With the perturbation equation, Equation (A10), and the boundary condition, Equation (A12), the similarity parameters can be identified as

$$\frac{1 - M_\infty^2}{(\gamma + 1) M_\infty^2 \tau\lambda} , \quad (\gamma + 1) M_\infty^2 \tau\lambda^3 , \quad (\gamma + 1) \lambda^2 , \quad \frac{\alpha}{\tau}$$

These parameters appear as coefficients in the equations defining the order of magnitude of their related terms. They can be identified as follows: the first one is the transonic similarity parameter K, the second one the square of the ratio of the length scales for the outer and inner regions, ϵ, the third one the swept back parameter, related to Γ_* and the fourth one the normalized angle of attack, related to σ_* (see Eqs. (1) and (4) in Section 2). Because of the retention of the right-hand side in Equation (A10), these parameters are not the same as those of the classical similarity. Different forms of small disturbance equations have been used in the literature on three-dimensional flows[11]. They are basically the same as Equation (A10) except that some terms in the right-hand side are dropped according to the author's preferences. If all terms at the right-hand side of the equation are dropped, the classical three-dimensional equation is obtained and the classical similarity law follows[10].

APPENDIX B

EVALUATIONS OF FUNCTIONS T(x), E(x) AND F(x) FOR A DELTA PLANFORM

For a planar wing at angle of attack the cross-flow potential given by the slender wing theory is[12]

$$\varphi = (a^2 - y^2)^{1/2} \tag{A13}$$

where a(x) is the contour of the leading edge.

The functions T(x), Equation (6) in Section 2, can be evaluated with the potential given in Equation (A13)

$$T(x) = \frac{1}{4\pi} \int_{-\infty}^{\infty} \int [\varphi(x,s)]_x \, [\varphi(x,y)]_x \, \ell n \left| \frac{1}{y - s} \right| ds \, dy$$

$$= \frac{a^2 a'^2}{\pi} \int_{-a}^{a} \frac{1}{(a^2 - y^2)^{1/2}} \left[\int_{-a}^{a} \frac{1}{(a^2 - s^2)^{1/2}} \ell n \frac{1}{|y - s|} ds \right] dy \tag{A14}$$

The integral with respect to s can be evaluated as

$$I_1 = \int_{-a}^{a} \frac{1}{(a^2 - s^2)^{1/2}} \ell n \frac{1}{|y - s|} ds$$

$$= - (\ell n \, a) \pi - \int_{-1}^{1} \frac{\ell n \, |\bar{y} - \bar{s}|}{(1 - \bar{s}^2)^{1/2}} d\bar{s}$$

$$= - (\ell n \, a) \pi - I_2$$

where $\bar{y} = \frac{y}{a}$ and $\bar{s} = \frac{s}{a}$.

To evaluate I_2 we differentiate I_2 with respect to $\bar{y}$

$$\frac{d I_2}{d\bar{y}} = \int_{-1}^{1} \frac{1}{(1 - \bar{s}^2)^{1/2}} \frac{1}{\bar{y} - \bar{s}} d\bar{s}$$

Let $\bar{s} = \cos\theta$, $\bar{y} = \cos\theta_1$ then

$$\frac{d I_2}{d\bar{y}} = \int_{o}^{\pi} \frac{d\theta}{\cos\theta_1 - \cos\theta} = 0$$

Hence I_2 = constant.

At $\bar{y} = 0$ the integral I_2 reduces to

$$I_2 = \int_{-1}^{1} \frac{\ell n \, |\bar{s}|}{(1 - \bar{s}^2)^{1/2}} d\bar{s}$$

Since the integrand is an even function of $\bar{s}$,

$$I_2 = 2 \int_0^1 \frac{\ell n \, |\bar{s}|}{(1-\bar{s}^2)^{1/2}} \, d\bar{s} = -\pi \ell n \, 2$$

Thus

$$I_1 = \pi \ell n \left(\frac{2}{a}\right)$$

And

$$T(x) = \frac{a^2 a'^2}{4\pi} \int_{-a}^{a} \frac{\pi \ell n \left(\frac{2}{a}\right)}{(a^2 - y^2)^{1/2}} \, dy$$

$$= \pi \ell n \left(\frac{2}{a}\right) a^2 \, a'^2 \qquad \text{(A15)}$$

The integral E(x), Equation (7) in Section 2, is evaluated as

$$E(x) = \frac{1}{4\pi} \int_{-\infty}^{\infty} [\varphi(x,s)]_y \, [\varphi(x,y)]_y \, \ell n \left| \frac{1}{y-s} \right| ds \, dy$$

$$= \frac{1}{\pi} \int_{-a}^{a} \frac{y}{(a^2 - y^2)^{1/2}} \left[\int_{-a}^{a} \frac{s}{(a^2 - s^2)^{1/2}} \, \ell n \left| \frac{1}{y-s} \right| ds \right] dy \qquad \text{(A16)}$$

The integral with respect to s is evaluated

$$I_1 = \int_{-a}^{a} \frac{s}{(a^2 - s^2)^{1/2}} \, \ell n \, \frac{1}{|y-s|} \, ds$$

$$= -a \left[\int_{-1}^{1} \frac{\bar{s}}{(1-\bar{s}^2)^{1/2}} \, \ell n \, |\bar{y} - \bar{s}| \, d\bar{s} \right]$$

$$= -a \, I_2$$

To evaluate the integral I_2 we again differentiate I_2 with respect to $\bar{y}$

$$\frac{d I_2}{d\bar{y}} = \int_{-1}^{1} \frac{\bar{s}}{(1-\bar{s}^2)^{1/2}} \, \frac{1}{|\bar{y} - \bar{s}|} \, d\bar{s}$$

Substituting $\bar{s} = \cos\theta$, $\bar{y} = \cos\theta_1$

$$\frac{d I_2}{d\bar{y}} = \int_{\bar{a}}^{o} \frac{\cos\theta}{|\cos\theta_1 - \cos\theta|} \, d\theta$$

$$= -\pi$$

Thus

$$I_2 = -\pi \bar{y}$$

and

$$I_1 = \pi y$$

The integral E(x) becomes

$$E(x) = \frac{1}{\pi} \int_{-a}^{a} \frac{y}{(a^2 - y^2)^{1/2}} (\pi y)\, dy$$

$$= \frac{\pi}{2} a^2 \qquad \text{(A17)}$$

Finally, the integral F(x) is evaluated as

$$F(x) = \int_{-\infty}^{\infty} [\varphi(x,y)]\, dy$$

$$= 2 \int_{-a}^{a} (a^2 - y^2)\, dy$$

$$= \pi a^2 \qquad \text{(A18)}$$

APPENDIX C

BOUNDARY CONDITION AT THE TUNNEL WALL

The linearized boundary conditions for flow past a perforated wall is given as[19]

$$u^* \pm \frac{1}{P^*} v^* = 0, \quad y^* = \pm h \tag{A19}$$

where P^* is the porosity factor depending on the physical configuration of the wall. The plus and the minus signs in the condition refer to the upper and the lower wall respectively. For the side walls, the velocity component w^* will replace v^* in the equation and the treatment is identical to the other walls. Introducing the velocity potential, Equation (A8), the condition can be written as

$$\frac{\partial \phi}{\partial x} \pm \frac{1}{P^*} \frac{\ell}{b} \frac{\partial \phi}{\partial y} = 0 \tag{A20}$$

In terms of the similarity variables defined in Equation (1), we have

$$\frac{\partial \phi}{\partial x} \pm \frac{1}{p} \frac{\partial \phi}{\partial \eta} = 0 \tag{A21}$$

where

$$P = \frac{P^* b}{\ell \tilde{\epsilon}} = \frac{P^*}{[(\gamma + 1) M_\infty^2 \tilde{\tau} \tilde{\lambda}]^{1/2}} \tag{A22}$$

Thus for flow similarity at the wall it is necessary to have P the same for both models. Since $\tilde{\tau}\tilde{\lambda}$ is the same for the models according to the first condition of Equation (26), the scaled porosity coefficient P will have the same value if the tests are performed at the same Mach number.

APPENDIX D

ESTIMATION OF OFF-SETTING FOR C_L vs α AND C_D vs C_L DATA

The off-setting of the C_D vs C_L polar from the zero lift axis is due to the asymmetry of the model about the central plane. With the angle of attack range of $-3°$ to $3°$, the data are fitted with a quadratic in the least square sense,

$$C_D = A + BC_L + CC_L^2 \tag{A23}$$

The minimum of C_D is thus

$$C_{D_m} = A - \frac{B^2}{4C} \tag{A24}$$

and the corresponding C_L is

$$C_{L_m} = -\frac{B}{2C} \tag{A25}$$

The angle of attack shift is taken to be the value of α at C_{L_m} by a linear fit through the data of C_L vs α.

$$C_L = D + E\alpha \tag{A26}$$

Thus

$$\alpha_m = \frac{C_{L_m} - D}{E} \tag{A27}$$

The data are then presented in the following forms

$$\begin{aligned} \bar{C}_L &= C_L - C_{L_m} \\ \bar{\alpha} &= \alpha - \alpha_m \\ \bar{C}_D &= C_D - C_{D_m} \end{aligned} \tag{A28}$$